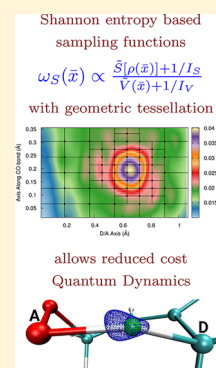# Efficient and Adaptive Methods for Computing Accurate Potential Surfaces for Quantum Nuclear Effects: Applications to Hydrogen-Transfer Reactions

Nicole DeGregorio and Srinivasan S. Iyengar*

Department of Chemistry and Department of Physics, Indiana University, 800 E. Kirkwood Avenue, Bloomington, Indiana 47405, United States

ABSTRACT: We present two sampling measures to gauge critical regions of potential energy surfaces. These sampling measures employ (a) the instantaneous quantum wavepacket density, an approximation to the (b) potential surface, its (c) gradients, and (d) a Shannon information theory based expression that estimates the local entropy associated with the quantum wavepacket. These four criteria together enable a directed sampling of potential surfaces that appears to correctly describe the local oscillation frequencies, or the local Nyquist frequency, of a potential surface. The sampling functions are then utilized to derive a tessellation scheme that discretizes the multidimensional space to enable efficient sampling of potential surfaces. The sampled potential surface is then combined with four different interpolation procedures, namely, (a) local Hermite curve interpolation, (b) low-pass filtered Lagrange interpolation, (c) the monomial symmetrization approximation (MSA) developed by Bowman and co-workers, and (d) a modified Shepard algorithm. The sampling procedure and the fitting schemes are used to compute (a) potential surfaces in highly anharmonic hydrogen-bonded systems and (b) study hydrogen-transfer reactions in biogenic volatile organic compounds (isoprene) where the transferring hydrogen atom is found to demonstrate critical quantum nuclear effects. In the case of isoprene, the algorithm discussed here is used to derive multidimensional potential surfaces along a hydrogen-transfer reaction path to gauge the effect of quantum-nuclear degrees of freedom on the hydrogen-transfer process. Based on the decreased computational effort, facilitated by the optimal sampling of the potential surfaces through the use of sampling functions discussed here, and the accuracy of the associated potential surfaces, we believe the method will find great utility in the study of quantum nuclear dynamics problems, of which application to hydrogen-transfer reactions and hydrogen-bonded systems is demonstrated here.

Shannon entropy based sampling functions

$$\omega_S(\vec{x}) \propto \frac{\tilde{S}[\rho(\vec{x})] + 1/I_S}{\tilde{V}(\vec{x}) + 1/I_V}$$

with geometric tessellation

allows reduced cost Quantum Dynamics

I. INTRODUCTION

Potential energy surfaces have critical significance in a wide range of areas in computational chemistry. Suitable examples include chemical reaction pathways where effective dynamical variables evolve along curvilinear paths to obtain (sometimes) large scale conformational and chemical transformations. Spectroscopic properties beyond the Harmonic approximation are obtained from eigenstates computed using potential surfaces. Hydrogen-transfer reactions[1] in atmospheric,[1−5] biological,[6−8] and materials[9−13] systems are often dictated by how solvent variables and collective reaction coordinates together influence the time-evolution of potential surfaces that dictate the hydrogen-transfer process; but computing these surfaces is a complex problem at the frontier of computational chemistry and chemical physics where the complexity grows exponentially with the dimensionality of the problem.

There exist multiple methods to determine the potential energy surfaces (PES) for complex systems.[14−18] Perhaps, one of the most powerful approaches involves the use of many-body expansions.[14,15,19−25] Many-body expansions involve one-body, two-body, and higher order interactions between the constituent parts of the system. These interactions include individual molecules, atoms, or aggregates of molecules, interactions between pairs of these, interactions between three or more such aggregates, and so on. The higher order interactions are adjusted to exclude overcounting by removing contributions from lower order interactions. Using permutationally invariant polynomials with many-body expansions[16,19,21−24] allows one to exploit the inherent (permutation) symmetry[26] in the system. The many-body expansions have also been employed to compute classical dynamics trajectories.[27] Despite this tremendous progress, the approach is best suited for uniform systems such as water clusters and becomes intractable to implement for general, chemical reactive problems such as those in biological and catalytic active sites.

In general there are two main factors that deeply hinder the problem of efficiently computing potential surfaces: (a) The number of potential energy evaluations grows exponentially with the size of the problem. (b) Each calculation can be quite expensive for a reasonable sized system especially when post-Hartree−Fock accuracy is desired. Classical[21−24,28−32] and quantum/classical[33−35] molecular dynamics have often been used to circumvent the scaling issues in point (a) above since dynamical trajectories sample important (classically allowed) regions of the potential and provide a first order approximation for a global potential surface. The problem in point (b) above represents a significant challenge, and there has been substantial

progress in the electronic structure community[20,27,36−66] that may, in the future, allow the accurate computation of potential surfaces in large systems. In this regard, several fragment-based *ab initio* molecular dynamics methods have recently been developed,[27,41,56,67−69] and these may, in the future, allow accurate and efficient calculation of potential surfaces.[67,68] Computing general potential surfaces with these protocols is an ongoing effort. Independently, machine learning[70−78] has become important in several communities and has been considered to have the potential to help circumvent the exponential scaling problem described above.

In this paper, we develop an alternative scheme, that has parallels to machine learning but is based on geometric tessellation of the high-dimensional potential surface through estimation of the spatially varying, or local, Nyquist frequencies[79] of potentials. Our approach is to construct a (rectangular and Voronoi diagrams[80,81] based) "tiling" of multidimensional space, where the size of each "hyperspace-tile" ideally depends on the local Nyquist frequency[79] of the potential, estimated using a set of targeted sampling criteria. Our sampling criteria depend on (a) the instantaneous quantum wavepacket density, (b) a crude approximation to the potential surface, its (c) gradients, and (d) a Shannon information theory based expression that estimates the local entropy associated with the quantum wavepacket. Using these sampling functions, the potential is recursively refined, but only targeted portions of the potential energy hyperspace are computed. The tessellation is achieved through a Boxcar[82] representation of the sampling function, and preliminary investigations of multidimensional tessellation are presented using Voronoi diagrams.[80,81,83]

The tessellation scheme is applied to compute potential surfaces in hydrogen-bonded systems and hydrogen-transfer reactions since the shared hydrogen nucleus in many such cases[1,6,35,84−95] shows unexpected quantum nuclear effects. These effects include very large experimentally observed primary kinetic isotope effects[6,35,90,96−108] and anomalous, nonclassical secondary isotope effects.[107−110] These problems require a detailed understanding of the potential surface experienced by a few degrees of freedom, that clearly display nonclassical behavior, while simultaneously considering the correlated effects arising from the change in configuration of the remaining parts of the system during the reactive process. For example in ref 35 it is shown that quantum nuclear effects such as H/D nuclear tunneling play a critical role in the hydrogen-transfer rate-determining step in soybean lipoxygenase-1 (SLO-1); furthermore, such a reactive process is nonadiabatic[35,106] in terms of coupling between the hydrogen-transfer dimensions and the larger-scale active site dynamics dimensions. The size of these systems requires a reduced dimensional study, and high level electronic structure treatment of such systems is cost prohibitive. Furthermore, in ref 108, it is noted that coupled hydrogen nuclear dynamics has a critical role in gauging experimentally observed nonclassical secondary kinetic isotope effects.[109] Correlated quantum nuclear description coupled to reaction coordinate dynamics is clearly very challenging. In addition to these problems, several anharmonic hydrogen-bonded systems that have the propensity to display multiwell characteristics[111−113] have also proven challenging to study accurately, and our approach here is geared toward these systems as well. Therefore, accurate and efficient methodologies to compute reduced dimensional potential surfaces in this regard are particularly critical for a

number of problems. The methods proposed here attempt to reduce the computational cost in obtaining accurate potential surfaces by reducing the number of electronic structure calculations that are needed to obtain the same. Future studies will combine these effects with molecular-fragmentation methods[20,38−48,51−53,58,59,62−69] to obtain high quality potential energy surfaces.

Here we demonstrate the methods proposed through the study of (a) the reduced dimensional potential surface encountered in the intramolecular hydrogen-transfer step in a hydrogen-bonded peroxy radical reaction intermediate that arises[114−116] during the OH-initiated oxidation of isoprene (a biogenic volatile organic compound[117−121]). Furthermore, to benchmark the optimal nature of the potential energy surface sampling procedures discussed here, we also (b) benchmark our sampling and tessellation schemes through the study of the highly anharmonic reduced dimensional potential energy surface associated with the shared proton in the bihalide ClHCl⁻ system, that has been a great challenge for several computational methods.[34,122−124]

This paper is organized as follows: In Section II our potential energy surface sampling condition and associated tessellation algorithm are presented. This involves both potential energy surface sampling and a recursive refinement process. Multi-dimensional tessellation measures are also introduced in Section II. Section III.A includes a comparison of errors between two different tessellation measures along with an analysis of computational gain. Specifically, these measures are (i) numerically benchmarked for accuracy and efficiency and (ii) used to compute effective hydrogen-transfer potential energy surfaces for transition states that are involved in a hydrogen-transfer reaction involving isoprene and (iii) quantum nuclear contributions to the reaction coordinate in the hydrogen-transfer process. The discussion is complemented by providing a background of the isoprene problem in Section III, which is then analyzed in Sections III.B and III.C. Appendix A provides a detailed discussion of interpolation procedures used here, whereas Appendix B provides benchmarks on the recursive refinement procedure. Conclusions are given in Section IV.

II. RECURSIVE REFINEMENT OF POTENTIAL SURFACES THROUGH ADAPTIVE, MULTIDIMENSIONAL, AND NONUNIFORM GEOMETRIC TESSELLATION WITH DETERMINISTIC MEASURE

As per the Nyquist-Shannon sampling theorem,[79,125,126] any function that is band limited in the frequency domain can be represented exactly using a finite number of samples in real space, provided the sampling rate is commensurate with the Nyquist frequency $(1/2\Delta)$ of the original function. This essentially implies that critical information from the continuous function is present in the aforementioned finite sample. Thus, the good news for potential energy surface fitting is that most potentials are "well-behaved" and smooth, with a relatively small number of non-negligible derivatives while remaining bounded in the frequency domain, and the potential energy surface ought to be well-represented by a finite sample in real space; but the associated bad news is that a sampling rate such as that described above is still extremely expensive to construct if accurate electronic structure methods are to be employed. However, it is also true that potential energy surfaces generally

have multiple length scales. Thus, while the lower energy region of a potential may be captured by low-frequency functions, the higher energy regions and classical turning points are best characterized through higher frequency functions. Hence, potential energy surfaces are generally nonisotropic and may, in some sense, possess *position dependent Nyquist frequencies*, or position dependent "ruggedness", that are best sampled through nonuniform grids where the grid spacing is to be determined by estimating the local frequency domain properties, as well as significance of the potential. To obtain such a nonuniform grid distribution, we first define the local Nyquist frequency, $\mathcal{N}(\bar{x}; \omega)$, of some function, $f(\bar{x})$, as the Fourier transform of a moving window filter acting on the function, that is

$$\mathcal{N}(\bar{x}; \omega) = \int d\bar{x}' \Theta(\delta - |\bar{x} - \bar{x}'|) f(\bar{x}') \exp(i\omega \bar{x}') \tag{1}$$

where $\Theta(\delta - |\bar{x} - \bar{x}'|)$ is a step function that is nonzero when $|\bar{x} - \bar{x}'| < \delta$. Furthermore, the ratio of $\mathcal{N}(\bar{x}; \omega)$ and the potential, that is

$$\frac{\mathcal{N}(\bar{x}; \omega)}{V(\bar{x})} = \frac{1}{V(\bar{x})} \int d\bar{x}' \Theta(\delta - |\bar{x} - \bar{x}'|) f(\bar{x}') \exp(i\omega \bar{x}') \tag{2}$$

reflects the local oscillation frequency of the potential damped by the value of the potential and is, hence, the desired local sampling rate in the sense that oscillatory and low energy regions of the potential are sampled at a higher frequency as compared to oscillatory and higher energy regions of the potential.

In this section, we present an algorithm to indirectly gauge the local, position dependent, Nyquist frequency of potentials to estimate the "optimal" sampling necessary for a reasonable and controllably accurate potential surface. The algorithm is iterative, involving two kinds of sampling functions that provide a measure of the necessary local sampling rate used to construct an "on-the-fly" potential fit, which is then iteratively improved until convergence. The method is benchmarked in Section III by computing reduced dimensional potential surfaces for (a) an anharmonic hydrogen-bonded system and (b) a hydrogen-transfer reaction of significance in atmospheric chemistry. In both cases the degrees of freedom pertaining to the hydrogen nuclear dimensions involved in the hydrogen bond and in the hydrogen-transfer process are treated quantum mechanically and represented using body-fixed Cartesian coordinates. The salient features of our algorithm to compute a potential energy surface for these reduced dimensional coordinates are as follows.

1. First, a crude estimate of the potential is constructed through a set of uniformly dispersed electronic structure calculations performed on a discretized grid that represents the domain of a multidimensional surface. At this stage one might use a lower level of theory (if the system is large semiempirical methods such as PM6 could be used), and, in this case, one might sample a large portion of the potential surface. This "lower level" potential surface is to be used as an initial guess for the next step to improve through recursive refinement. Future studies will also gauge the use of classical AIMD simulations at this stage.

2. For the surface computed in the previous step, eigenstates are obtained. We use the Arnoldi approach to compute eigenstates[127,128] since the matrix sizes are expected to be large. The Arnoldi approach differs from the well-known Lanczos

iterative scheme,[129] in that any function of the Hamiltonian can be used to construct a Krylov-like basis,[130] instead of the Hamiltonian itself. These procedures converge rapidly to eigenstates in a specified neighborhood.

3. Next a sampling function[34,82,124,131] is constructed using a propagated wave packet (or an eigenstate), the potential surface computed in the previous step, and gradient of the potential. Two versions of the sampling are considered in this publication, namely

$$\omega_S(\bar{x}) \propto \frac{\tilde{S}[\rho(\bar{x})] + 1/I_S}{\tilde{V}(\bar{x}) + 1/I_V} \tag{3}$$

$$\omega_\rho(\bar{x}) \propto \frac{[\tilde{\rho}(\bar{x}) + 1/I_\rho][\nabla_{\bar{x}}\tilde{V}(\bar{x}) + 1/I_{V'}]}{\tilde{V}(\bar{x}) + 1/I_V} \tag{4}$$

where $\{\bar{x}\}$ represents the coordinate representation pertaining to the quantum nuclear degrees of freedom. Since in this paper we aim to compute reduced dimensional surfaces, Cartesian coordinates are employed to describe $\{\bar{x}\}$, but these measures can be easily generalized to other coordinate systems. Furthermore, the wave packet density, ρ, the potential, V, gradient of the potential, $\nabla_{\bar{x}} V(\bar{x})$, and the *local* Shannon entropy function computed from the quantum wave packet density, $S[\rho(\bar{x})] \equiv -\rho(\bar{x}) \log(\rho(\bar{x}))$, are all normalized, scaled, and shifted according to

$$\tilde{\rho}(\bar{x}) = \frac{\rho(\bar{x}) - \rho_{\min}}{\rho_{\max} - \rho_{\min}} \tag{5}$$

where $\rho_{\min}(\rho_{\max})$ are the minimum(maximum) values for the wave packet density and similarly for $\tilde{V}$, $\nabla_{\bar{x}}\tilde{V}$, and $\tilde{S}[\rho(\bar{x})]$. This results in balanced contributions from each physical quantity. Furthermore, both sampling functions above remain positive semidefinite under this choice. Equation 4 is identical in form to the time-dependent deterministic sampling (TDDS) function developed in ref 33 for use in quantum nuclear dynamics. Here we use this measure to compute potential surfaces within a recursive paradigm. The three integers I_ρ, $I_{V'}$, and I_V are chosen to be 1, 3, and 1, respectively, as outlined through analytical and numerical considerations in ref 82. We require the function ω_ρ to have equal sampling in the classically allowed and classically forbidden regions of the potential, and this condition and this alone in ref 82 leads to the mentioned values of I_ρ, $I_{V'}$, and I_V. The parameter, I_S, is chosen to be equal to I_ρ as suggested in ref 131.

The general form of Shannon entropy[125]

$$-k \int d\bar{x} \rho \log(\rho) \equiv k \int d\bar{x} S[\rho(\bar{x})] \tag{6}$$

educates our choice in eq 3. Here ρ is the probability of finding a system in realization (or microstate represented by) $\bar{x}$, and k is a proportionality constant (Boltzmann constant in thermodynamics and simply the identity, *i.e*, $k = 1$, in information theory[132]). Here, we refer to $S[\rho(\bar{x})]$ as the "local Shannon entropy" because, while the full sum in eq 6 is the Shannon entropy,[125] $S[\rho(\bar{x})]$ implicitly depends on the realization or local value of the variable $\bar{x}$.

The choice in eq 4 is due to the need to appropriately represent classical turning points, where the gradient of the potential is generally high and hence quantum effects, such as tunneling, develop. In addition, the choice of $\omega_\rho(\bar{x})$ was, in refs 82 and 34, influenced by its connections to the quantity
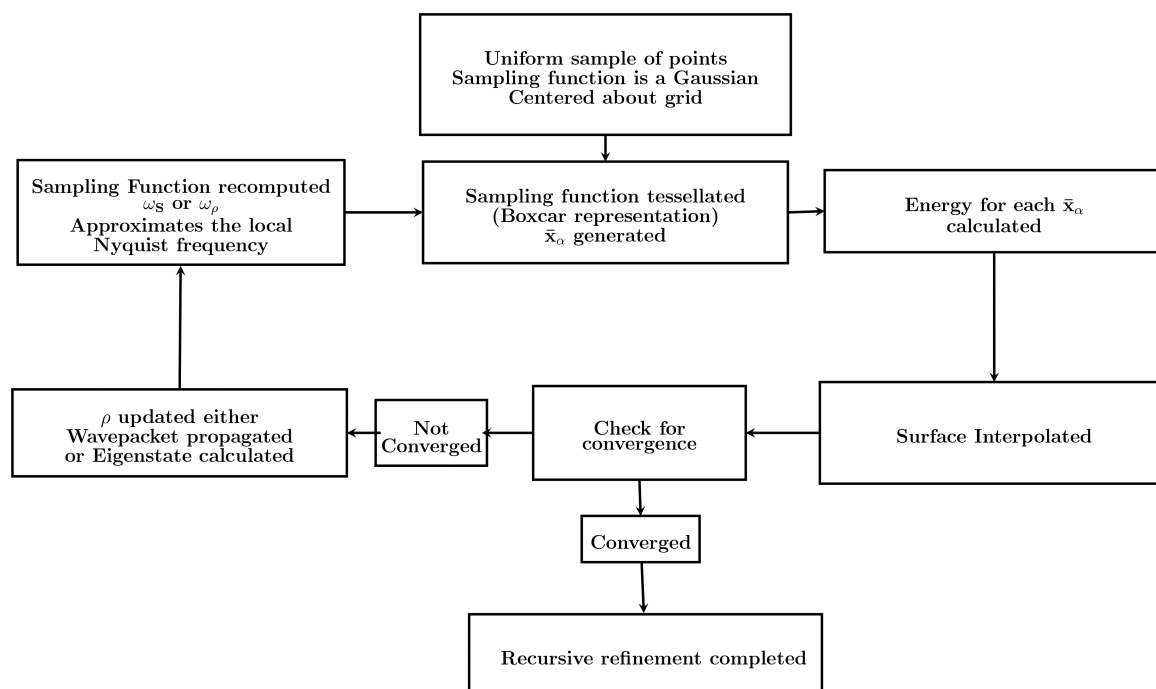
Figure 1. A graphical representation of the recursive refinement procedure.

$$\left(\frac{1}{E - V(x)}\right)\frac{\partial V}{\partial x} \tag{7}$$

which appears in WKB theory,[133] which holds under the condition

$$\frac{p}{\hbar} \equiv \bar{\lambda}^{-1} \gg \left(\frac{1}{E - V(x)}\right)\frac{\partial V}{\partial x} \tag{8}$$

One objective of the sampling function, $\omega_\rho(\overline{x})$, is to provide a larger sample in the rapidly varying region of the potential, which is generally a region where the WKB approximation breaks down. Furthermore, it has been shown numerically[34,82] that $\omega_\rho(\overline{x})$ is directly proportional to the Bohmian quantum potential,[133−145] which is again a signature of quantum-mechanical effects. In Section II.B we also numerically gauge the connections between eqs 3 and 4 and the local Nyquist frequency of the potential defined in eq 1.

4. Once the sampling functions are computed on a grid that represents the quantum nuclear degrees of freedom, the next step is to divide this multidimensional space into regions of significance (or multidimensional *tiles*) based on weights given by the sampling functions. Toward this, a Dirichlet tessellation[146] of the multidimensional potential energy surface is constructed using $\omega_S(\overline{x})$ and $\omega_\rho(\overline{x})$ as grid weights. Details regarding this procedure are given in Section II.A. There are several approaches one can use here, and perhaps the most common methods for multidimensional tessellation is the Voronoi diagram.[80,81,83] However, for reasons that will be discussed in Section II.A, here we also use a Boxcar representation of both sampling functions to reduce the two sampling functions into multidimensional, rectangular, *tiles*, or domains in space with similar local length scales (or inverse Nyquist frequencies). Numerical illustrations that inspect the relation between $\omega_S(\overline{x})$, $\omega_\rho(\overline{x})$, and the local Nyquist frequency are provided in Section II.B. Using these methods, we effectively construct a rectangular tiling of the multidimensional surface, where the size of each "hyperspace-tile" depends on the sampling measures $\omega_S(\overline{x})$ and $\omega_\rho(\overline{x})$, and the integral of the sampling functions inside each *tile* is roughly constant. *One may also think of these tiles as being representative of multidimensional sampling rates and hence an indirect signature of the local Nyquist frequency.* In our case, these sampling rates are obtained using eqs 3 and 4.

5. Once the tiling is complete, we have facilitated a quantum-mechanical grid compression. Depending on the method of tiling (Boxcar or Voronoi), electronic structure calculations are either performed at a chosen subset of vertices of the hyper-rectangular tiles obtained from the Boxcar representation (see Figure 3 and associated discussion in Section II.A) or the center of the irregular polyhedra (polytope in higher dimensions) obtained from Voronoi decomposition (see Figure 2 and associated discussion in Section II.A). At the end, approximately one electronic structure calculation is performed to represent each hyper-rectangular *tile* or polytope. These calculations are then used to compute estimates for the potential surface. While in this paper we limit ourselves to DFT treatment, at this juncture it is possible to hierarchically increase the level of theory and include MP2 or use fragmentation techniques[67−69] to obtain approximations for higher levels of theory. As we will see, the grid compression is several orders of magnitude and results in large computational gains. Furthermore, the number and size of *tiles* depends on the local variations of the potential and not explicitly on the dimensionality of the quantum nuclear degrees of freedom. Following the computation of electronic energy and gradients at the set of points given by the Boxcar representation of ω_S and ω_ρ, an interpolation is constructed to obtain the full potential surface at all values of $\{\overline{x}\}$. Here multiple methods have been employed for this purpose. All interpolation schemes are standard protocols available in the literature. The relevant parameters and other details about the interpolation procedures used in this work are provided in Appendix A.
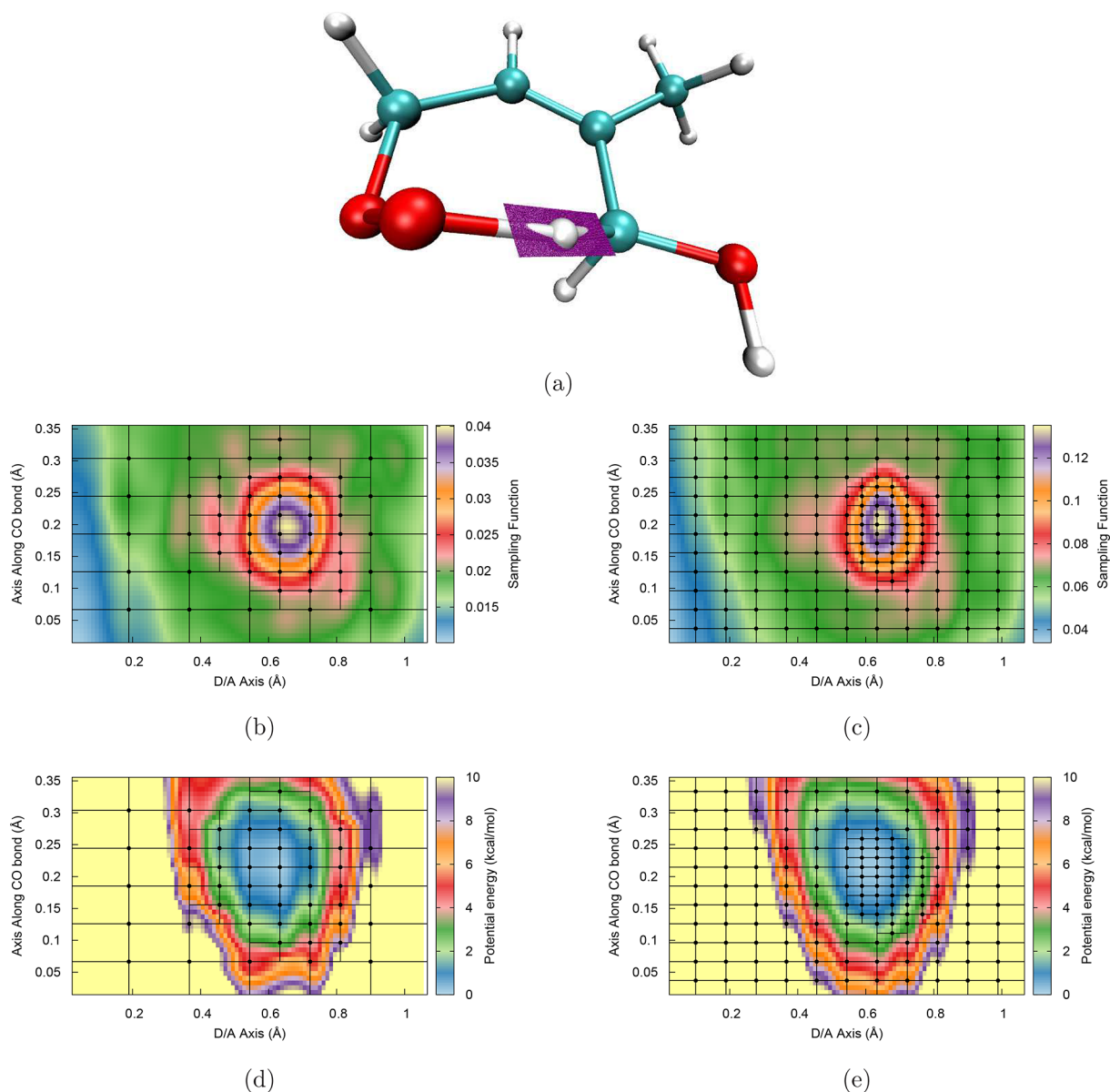
Figure 2. Illustration of the sampling function, ω_S, in eq 3. Parts (b) and (c) represent a sampling function in two-dimensions for the system shown in part (a). Also superimposed in parts (b) and (c) are the grids obtained from the Boxcar representation of the sampling function. The sampling function is tessellated into 78 *tiles* [(b) and (d)] and 205 *tiles* [(c) and (e)]. Electronic structure energies and gradients computed at the vertices of these *tiles* are used to interpolate on a grid with ≈5000 points, and the resultant potentials are shown in parts (d) and (e). The accuracy is of the order 1/100-th kcal mol^{-1} as shown in later sections.

6. Once the potential is computed, an initial wavepacket is propagated on this potential for a few steps and employed as the wavepacket to compute the sampling functions for the next iteration. At this stage it is also possible to use the eigenstates of the potential instead of using quantum propagation.

7. Next, the algorithm cycles back to step 2 and iterates to convergence. A critical aspect of the steps here is that multiple electronic structure packages can be used within one single calculation. These aspects will be gauged and studied in future publications. The method is illustrated through the flowchart in Figure 1.

II.A. Geometric Tessellation of the Potential Surface Using $\omega_S(\overline{x})$ and $\omega_\rho(\overline{x})$. Given a conformational space represented using the coordinates $\{\overline{x} \equiv \{\overline{x}_i\}\}$, in Step 4 in the algorithm discussed in the previous section, one needs to find a discrete sample of points, $\{\overline{x}_\alpha\}$, that will be used to

suitably represent a potential surface depicted in the domain $\{\overline{x}\}$. We wish to find $\{\overline{x}_\alpha\}$ by using $\omega_S(\overline{x})$ and $\omega_\rho(\overline{x})$ as measures that represent the significance of each $\overline{x}$. Furthermore, the family of $\{\overline{x}_\alpha\}$, once found, provides a conduit to tessellate or divide the $\{\overline{x}\}$-space.

One possible method to achieve this tessellation process is to employ a multidimensional Boxcar representation of the sampling functions, $\omega_S(\overline{x})$ and $\omega_\rho(\overline{x})$, where the individual Boxcar regions, or *tiles*, are expected to represent local Nyquist frequencies (see Section II.B). An illustration of the Boxcar representation is provided in Figure 2 for the hydroxy-peroxy isoprene system treated in Section III. An additional constraint imposed on the Boxcar representation of $\omega_S(\overline{x})$ and $\omega_\rho(\overline{x})$ is the fact that as the number of *tiles* requested, or the number of $\{\overline{x}_\alpha\}$ sample-points requested, increases, both $\omega_S(\overline{x})$ and $\omega_\rho(\overline{x})$ must be gradually modified in the direction of a uniform
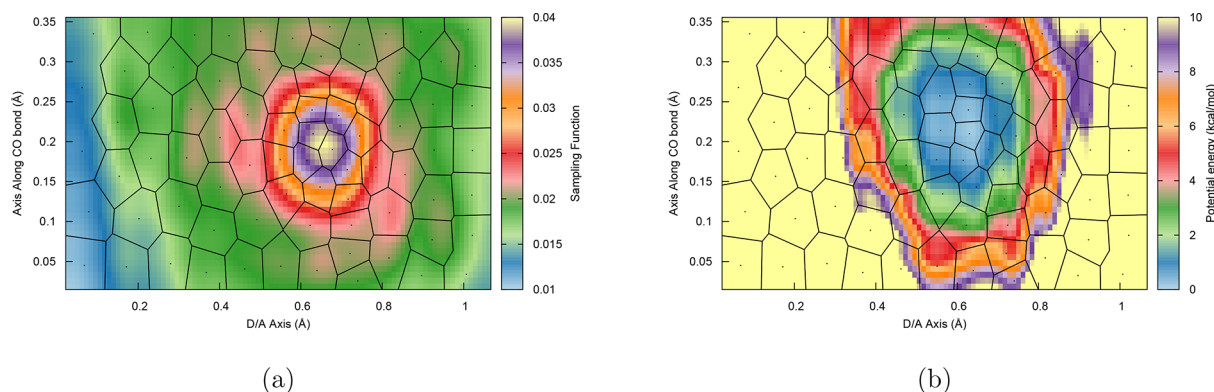
(a) (b)

Figure 3. Illustration of the sampling function, ω_S, in eq 3. The sampling function shown in Figure 2(b) is tessellated here using Voronoi diagrams.[83] Part (a) here shows the Voronoi tessellation in conjunction with ω_S, whereas part (b) shows the associated potential surface.
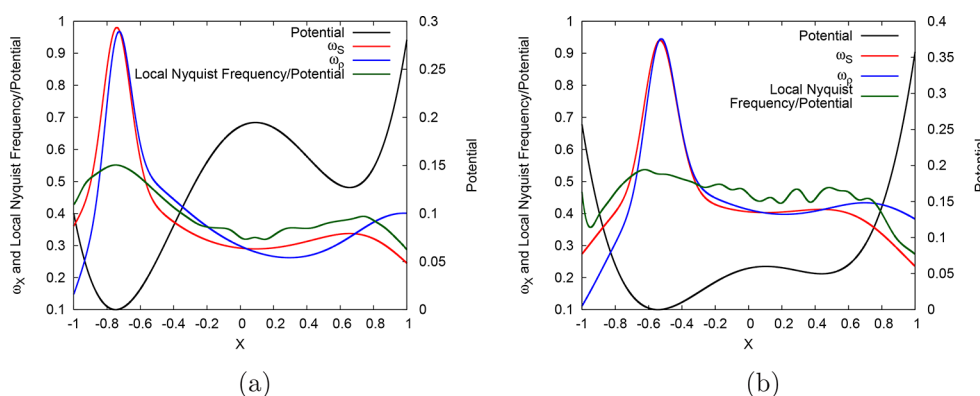

(a) (b)

Figure 4. Parts (a) and (b) show two different double potentials (black) and associated behavior of the quotient of the local Nyquist frequency and potential in eq 2 (in green). As expected these indicate greater contributions in the classically allowed regions. We also present the sampling functions shown in eqs 3 and 4, and similarities between these and $\mathcal{N}(\bar{x})$ in eq 2 are gauged by computing correlations presented in Figure 5.
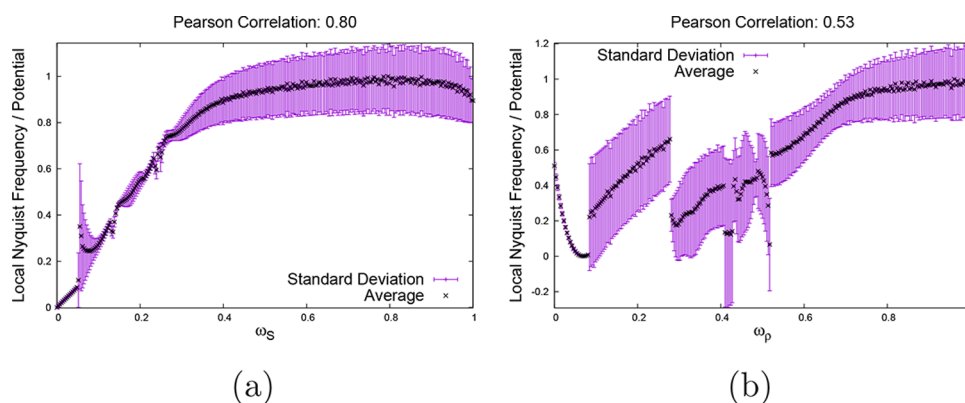

(a) (b)

Figure 5. Parts (a) and (b) represent the correlation between $\omega_S(\bar{x})$ [(a)] and $\omega_\rho(\bar{x})$ [(b)] with the local Nyquist frequency descriptor in eq 2. Both potentials from Figure 4 are used, and the averages are presented here. Based on these figures, it appears that $\omega_S(\bar{x})$ correlates better with the local Nyquist frequency. This aspect is also consistent with our numerical studies later in the paper, where we show that $\omega_S(\bar{x})$ based sampling does indeed represent the potential better.

distribution of $\{\bar{x}_\alpha\}$. A procedure to carry out this process is discussed in ref 82, and, as noted, the resultant representation is shown in Figure 2.

Another approach for multidimensional tessellation is to use Voronoi diagrams[80,81] to divide the region using the sampling functions. This method is briefly illustrated in Figure 3. However, as seen by visual inspection of the Figure 3(a) and Figure 2(b), and also Figure 3(b) and Figure 2(d), the Boxcar representation appears to capture the sampling function better. In addition, the rectangular grid obtained from the Boxcar

representation is more commensurate with employing multidimensional Hermite-curve interpolation, which is the method of choice in this publication.

II.B. Rationale Behind the Choice in Eqs 3 and 4. In this section we gauge the connections between $\omega_S(\bar{x})$, $\omega_\rho(\bar{x})$, and the local Nyquist frequency estimates, or "optimal" sampling rate estimate, $\frac{\mathcal{N}(\bar{x};\omega)}{V(\bar{x})}$ in eq 2. In Figure 4 we compare ω_S and ω_ρ with the $\frac{\mathcal{N}(\bar{x};\omega)}{V(\bar{x})}$. As shown in eq 1, the local Nyquist frequency,
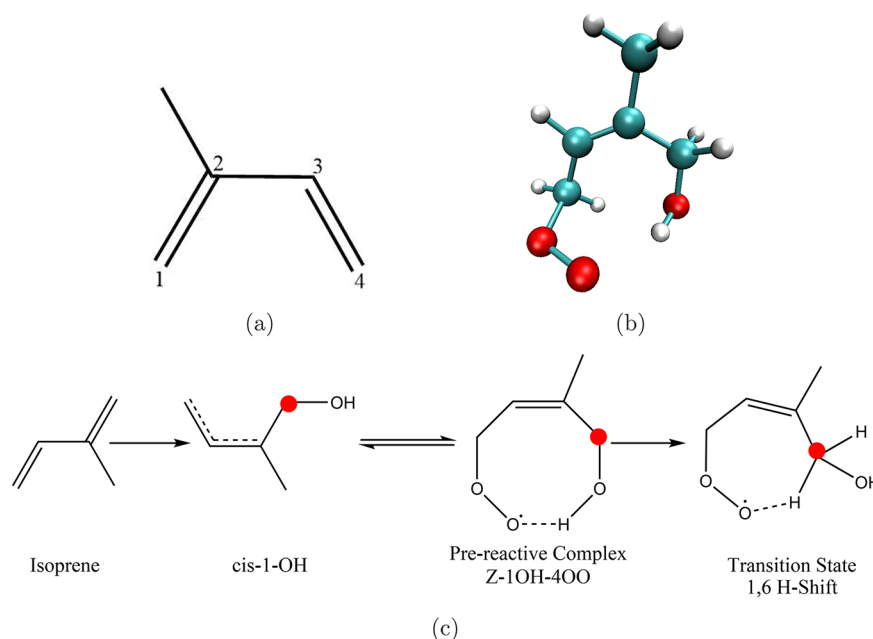
Figure 6. (a) Isoprene, (b) the hydrogen-bonded hydroxy peroxy radical, and (c) the reaction pathway connecting the two, with donor carbon shown in red. The last structure in part (c) represents the transition state involved in the hydrogen-transfer process. See Figure 7 for possible forms of this structure with barrier heights shown in Table I.

$\mathcal{N}(\overline{x}; \omega)$, is computed from the Fourier transform of a moving window filter acting on the potential. In Figures 4 and 5, we have used the eigenstate of the displayed potential in computing ω_S and ω_ρ. This is done for illustrative purposes. We find that the desired sample rate, $\frac{\mathcal{N}(\overline{x};\omega)}{V(\overline{x})}$ in eq 2, is in general positively correlated with ω_S to a greater extent as compared to ω_ρ as noted in Figure 5. The Pearson correlations are noted in these figures. It is, however, important to note that while the desired sampling rate generally correlates quite well with ω_S, larger values of the desired sampling rate are presented with a multiplicity of values of ω_S (all of which are high) as is clear from the asymptotic flattening of the curve in Figure 5(a). This difference arises in the minimum energy region of the potential as may be clear upon inspection of Figure 4 but is not significant since the sampling rate obtained from ω_S is generally higher in this region as compared to other regions, as may also be clear from Figure 4. In fact, when the correlation in Figure 5(a) is recomputed by ignoring the flat region, the Pearson correlation is 0.99. The quantity ω_ρ correlates to a much lesser extent as compared to ω_S. This difference is carefully probed in the examples considered in the results section. While one needs to know the potential to compute the local Nyquist frequency based desired sampling rate, the sampling functions in eqs 3 and 4 can be computed before the potential is known, as discussed in the algorithm outlined in Section II, and hence the numerical similarities between these is quite appealing.

The remaining portion of the paper is organized as follows. In the next section we first illustrate the sampling function for a simple bihalide hydrogen-bonded system. In lower dimensions we illustrate the potentials obtained from all four different fitting procedures (Appendix A) along with the sampling functions and the true potential. In high dimension, we are in a position to compare the efficiency and accuracy of the fitting methods for the irregular grid samples obtained from eqs 3 and 4. Additional benchmarks related to the recursive refinement procedure are presented in Appendix B. Following this we

consider a hydrogen-transfer reaction in a biogenic volatile organic compound called isoprene. It has been noted in recent publications[114−118,120,121,147,148] that isoprene, which is a terpene, reacts with dioxygen, and the resultant compound can reorganize affecting the branching ratios of the products obtained. A brief background of this problem is provided in Section III with results from potential energy surface calculations.

III. NUMERICAL BENCHMARKS ON ACCURACY OF POTENTIAL SURFACES OBTAINED FROM THE DIRECTED MEASURE FUNCTIONS, ω_S AND ω_ρ

We benchmark the sampling functions in conjunction with performance for the four different fitting procedures described in Appendix A. The systems under study include (a) the highly anharmonic potential that is experienced by the shared proton in the bihalide $[\text{ClHCl}]^-$ system and (b) a hydrogen-transfer prereactive configuration involved in the oxidation of isoprene, a biogenic volatile organic compound. The $[\text{ClHCl}]^-$ system, despite its size and availability of the associated highly accurate experimental velocity-modulation spectroscopy results,[149] presents a significant challenge to most state-of-the-art methods[122,123] due to the coupled dynamics of the shared proton and the heavier, donor/acceptor chlorine atoms.[34] Quantum wavepacket *ab initio* molecular dynamics (QWAIMD)[34,124] has been used to study this problem in some detail, and here, we consider this system as a suitable challenge for the preliminary studies in this section.

The hydroxy-peroxy isoprene system shown in Figure 6(b) is a proposed intermediate of the Leuven Isoprene Mechanism (LIM1)[114−116] used to explain the higher than expected OH-radical concentration found during recent air-pollutant monitoring campaigns.[121] Here, an internal hydride transfer (Figure 6(c)) eventually leads to the regeneration of the OH radical under low NO_X conditions[114] common in rainforest areas[117,118,120,147,148] and appears to explain the experimental results in ref 121. The prereactive system for this internal
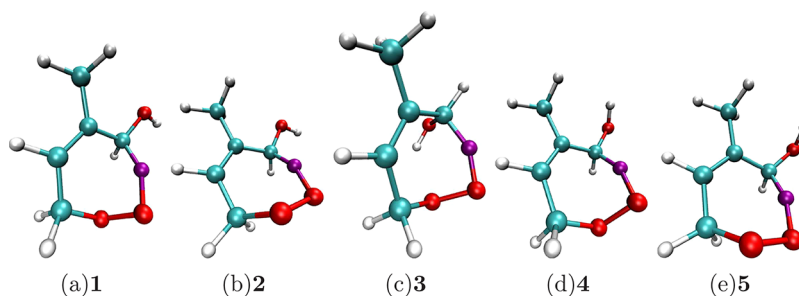
Figure 7. Transition states corresponding to the structure marked "Transition State 1,6 H-Shift" in Figure 6(c). Structures labeled "1" and "3" are similar to those proposed in ref 114 that lead to mechanisms that deviate from the traditional reactions and affect the production of tropospheric ozone, a critical constituent of photochemical smog. The transferring hydrogen atom is marked in purple. The number in bold is the assigned number for the transition state that is used throughout the rest of the paper.

Table I. ZPE Corrected (within Harmonic Approximation) Barrier Heights (in kcal/mol) Associated with the Transition States Shown in Figure 7

	B3LYP/6-311++g(d,p)				M062x/6-311++g(d,p)				MP2/6-311++g(d,p)			
TS	E^a ($\frac{kcal}{mol}$)	D/A^b (Å)	CHO^c	COO^d	E^a ($\frac{kcal}{mol}$)	D/A^b (Å)	CHO^c	COO^d	E^a ($\frac{kcal}{mol}$)	D/A^b (Å)	CHO^c	COO^d
1	16.67	2.48	150.49	85.74	19.82	2.46	147.67	84.86	23.38	2.45	162.02	93.96
2	17.78	2.52	157.09	99.60	21.42	2.50	154.97	99.33	27.01	2.45	162.27	94.24
3	17.25	2.48	151.81	86.00	19.50	2.45	149.42	85.56	21.31	2.44	154.47	88.70
4	18.04	2.49	152.57	87.28	21.00	2.46	149.03	85.89	23.10	2.45	161.28	97.54
5	18.75	2.52	159.76	99.25	22.17	2.50	158.00	98.71	21.32	2.44	154.47	88.70

^{a}The energy noted here is the difference between the ZPE corrected prereactive complex energy for the structure shown in Figure 6(b) and the ZPE corrected transition state energies of the structures in Figure 7. ^{b}The columns labeled D/A show the donor−acceptor distance in Å. ^{c}The columns marked CHO show the angle between the angle in degrees between the donor, transferring hydrogen, and acceptor. ^{d}The columns labeled COO show the angle in degrees between the donor carbon, acceptor oxygen, and the additional oxygen from the added O_2 group.

hydride shift is stabilized by an intramolecular hydrogen-bonded ring formation as shown in Figure 6(b). A few transition states arising from the prereactive complex in Figure 6(b) (also see Figure 6(c)) that support hydrogen transfer are shown in Figure 7, and the transferring hydrogen atom is shown in purple. Relative energies for the structures in Figure 7, with respect to the prereactive complex in Figure 6(b), are provided in Table I. (Also see ref 116.)

As part of our studies here, we inspect the quantum nuclear effects arising from the shared proton in Figure 7. As seen from Table I, the barrier heights for these states are quite close, and hence one may expect all of these to be (perhaps statistically) populated during the hydrogen-transfer process. Furthermore, structures labeled "1" and "3" are similar to those found in ref 116. To support this analysis we compute potential surfaces experienced by the transferring hydrogen atom using the algorithm presented. The body-fixed reference frame used to depict the quantized hydrogen nucleus is shown in Figure 8.
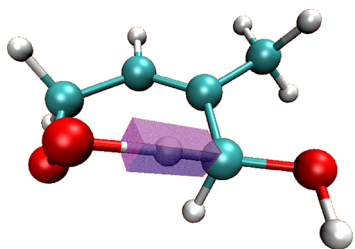

Figure 8. Body-fixed reference frame that represents the quantized nucleus is shown in purple. The associated three-dimensional grid encompasses the region inside this purple box. Note that this grid is a three-dimensional generalization of the one presented in Figure 2(a).

Here the purple box is used to represent a multidimensional grid, and each grid point represents a unique molecular geometry where the potential energy and gradients are to be evaluated. We will employ the techniques proposed in Section II to compute these potential energy surfaces at much reduced computational effort.

III.A. Benchmarking the Fitting Functions Used in Conjunction with the Sampling Functions, ω_S and ω_ρ: Numerical Studies on ClHCl⁻. As noted earlier, in this section we benchmark the accuracy and efficiency of all four fitting procedures listed in Appendix A and used in conjunction with the local Nyquist frequency estimates, $\omega_S(\bar{x})$ and $\omega_\rho(\bar{x})$. The system for the studies in this section is ClHCl⁻, where the potential surface is to be computed for the reduced dimensions pertaining to the shared proton. Two-dimensional and three-dimensional real-space representations of the quantized degree of freedom (the shared proton in ClHCl⁻) are considered here. The grid occupies a 0.80 Å domain in each direction, namely the donor−acceptor direction and the two orthogonal dimensions. To accurately capture the real space wave functions and potentials, the region is discretized to obtain an equally spaced grid containing 49 grid points along the donor/acceptor axis and 49 along all orthogonal directions. This amounts to a grid spacing of approximately 0.017 Å in each direction, and the region depicting the grid is quite similar to that shown in Figure 8 for hydroxy-peroxy isoprene. We, thus, have 117649 grid points in three-dimensions and 2401 grid points in two dimensions, where estimates for the electronic structure potential are needed. Toward this, we utilize $\omega_S(\bar{x})$ and $\omega_\rho(\bar{x})$ along with the aforementioned tessellation scheme to divide the surface into critical regions and determine a small set of sample points where electronic structure calculations are
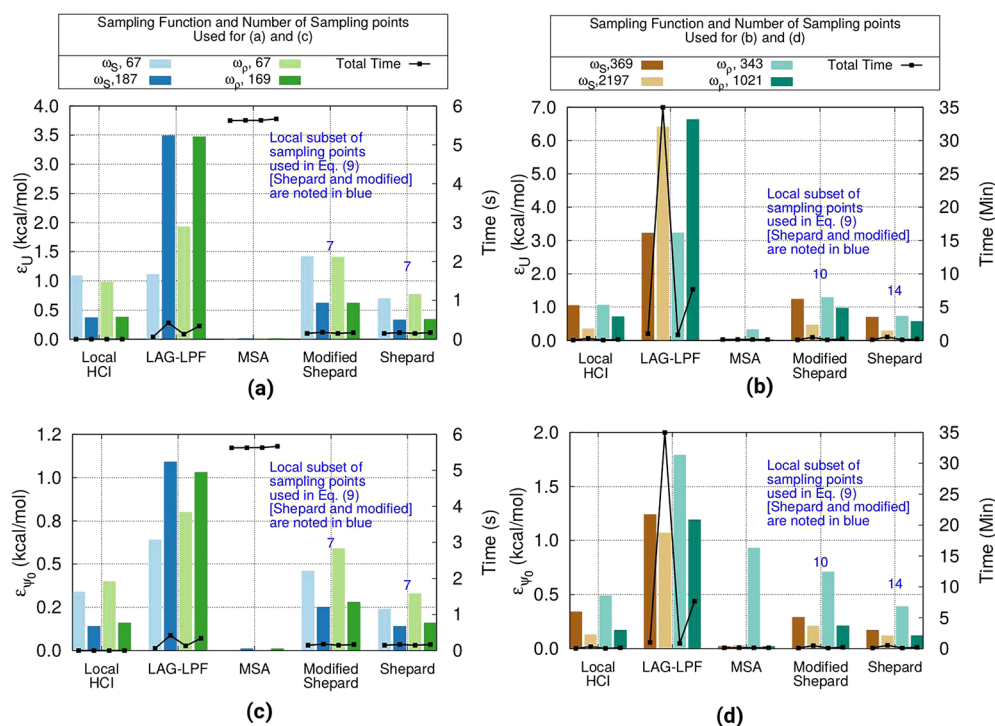
Figure 9. Error analysis (eqs 9 and 10) and computational gain in obtaining the shared proton potential surface for ClHCl⁻ using ω_S and ω_ρ. The legend above parts (a) and (b) shows the sampling function and the number of sampling points used to fit the surfaces. Two different cases are presented for each fitting function and each sampling function. The numbers in blue recorded above the Shepard interpolation data are the size of the local subset discussed after eq A2. Part (a) shows ϵ_U (eq 9) for a two-dimensional surface with a total of 2401 interpolated grid points resulting in a 36-fold and 13-fold reduction in electronic structure calculation time when using ω_S (36-fold and 14-fold reduction using ω_ρ). Part (b) shows ϵ_U (eq 9) for a three-dimensional surface with a total of 117649 interpolated grid points resulting in a 319-fold and 54-fold reduction in the number of electronic structure calculations when using ω_S (343-fold and 115-fold reduction using ω_ρ). Parts (c) and (d) show the associated ϵ_ψ from eq 10 for the 2D and 3D surfaces analyzed in (a) and (b) respectively. The eigenstate used here is the hydrogen ground state.

performed and used to obtain the potentials on the remaining number of grid points discussed above through interpolation. Typically, in this section we gauge the accuracy of the procedure by performing only 369 electronic structure calculations spread over the grid with locations determined from the tessellation conditions. These are then interpolated to 117649 three-dimensional grid points. In two dimensions we gauge the accuracy from 67 electronic structure calculations interpolated to the grid comprising 2401 points. In both cases a larger number of sample points is considered to check convergence of surface. However, to check the accuracy, we also need a reference electronic structure surface on the full grid which is clearly a formidable task even for this small system, given that 117649 calculations are required for the three-dimensional case. Hence the electronic structure method used in this section is PM6. The convergence of the recursive refinement technique used here is demonstrated in Appendix B.

The accuracy of the recursive refinement calculations is computed as follows. The potential computed on a set of sampled points is extrapolated to obtain $V_{approx}(\overline{x})$. This is then compared with the reference PM6 calculations on the full grid. While the mean absolute deviation between the approximate and full reference surfaces

$$\epsilon_U = \frac{1}{N} \sum_i |V_{approx}(\overline{x}_i) - V_{ref}(\overline{x}_i)| \tag{9}$$

provides a global error, a ground eigenstate weighted form of the same

$$\epsilon_{\psi_0} = \sum_i |\psi_0(\overline{x}_i)|^2 |V_{approx}(\overline{x}_i) - V_{ref}(\overline{x}_i)| \tag{10}$$

provides the cumulative error in localized regions that are populated by the ground state wave function.

Figures 9(a) and 9(b) show the accuracy and the CPU time required to carry out the recursive refinement procedure for two-dimensional and three-dimensional versions of the shared proton potential surface in ClHCl⁻. Due to the large size of the associated matrices, we have employed the Arnoldi iterative diagonalization procedure[127,128] to compute eigenvalues and eigenfunctions. As noted in each case, the left-vertical axis represents either ϵ_U (eq 9) or ϵ_{ψ_0} (eq 10), in kcal/mol, and the right-vertical axis shows the CPU time. The number of potential energy sampling points, that is the number of electronic structure calculations performed to obtain the reduced dimensional potential surface, is also mentioned in the figure legend. For example, when the number of electronic structure calculations is increased from 67 to 167 in the two-dimensional case, the ϵ_{ψ_0}-error reduces from roughly 0.35 kcal/mol to 0.1 kcal/mol when the local version of Hermite curve interpolation is used. Note that these electronic structure calculations are then used to interpolate the value of the potential on 2401 points as explained in the caption of Figure 9. Similarly, for the three-dimensional case, the ϵ_{ψ_0}-error reduces from approximately 0.2 kcal/mol to 0.1 kcal/mol when the number of sample points is increased from 369 to 2197 and when Shepard interpolation is used to interpolate onto the full 117649 grid points.

In all cases, the CPU time shown in Figure 9 is the total time needed to generate the sampling functions and compute approximations to the full surface but does not include the time spent for the electronic structure calculations. Upon further inspection of Figure 9, it follows that Lag-LPF (eq A1) has the largest error, and this error increases with a larger number of sampling points. This is presumably due to the fact that the low-pass filtering in eq A1 does not completely eliminate the Runge oscillations,[150] and these accumulate causing large deviations throughout the potential. In eq A1, as the number of sampled points, indexed "i", increases, the polynomial order in x increases which raises the oscillation frequencies built in $f(x)$. The local Hermite curve interpolation and the Shepard interpolation methods have largely reduced error as compared to Lag-LPF, but the best results are obtained from MSA.[21] However, there are developments that remain in being able to use MSA for general reduced dimensional surface calculations such as those undertaken in the next subsection.[151] Hence we use Hermite curve interpolation with Boxcar tessellation for the remaining portion of this paper.

III.B. Analysis of the Hydroxy-Peroxy Isoprene Hydrogen-Bonded Intermediates Shown in Figure 7. Section III.A, Figures 9 and 10, and Appendix B demonstrate the robust
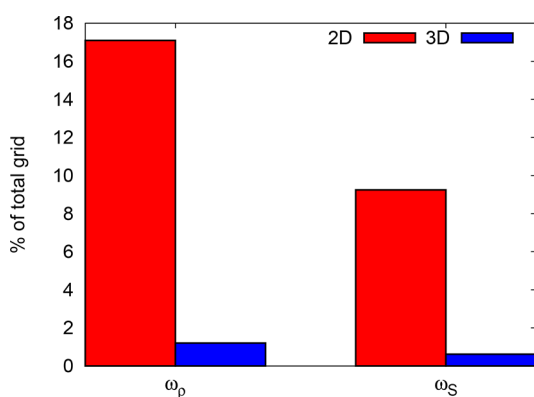

Figure 10. Reduction in computational complexity as a result of recursive refinement is measured in terms of reduction in the number of electronic structure calculations.

and efficient nature of the recursive refinement procedure when used in conjunction with eqs 3 and 4 and the accompanying tiling mechanism. In this section, we utilize the approach to gauge the contributions from quantum nuclear effects toward all five transition states shown in Figure 7. Each transition state used the grid configuration shown in Table II and also used in Appendix B. The potential energy surfaces are computed on the set of sampling points noted in Table II, obtained using ω_S, and interpolated to the full-grid using local Hermite curve interpolation. The level of theory includes both B3LYP/6-311++g(d,p) and M062x/6-311++g(d,p). For each case the potential surfaces are used to construct eigenstates as discussed in Section III.A. These ground eigenstates are then used to compute product state probabilities which we represent as transmission amplitudes in Table III. For all five of the transition states the transmission (or product-side) probability is greater than 60% for both levels of electronic structure theory considered here. This significant population transfer noted in Table III is analyzed in greater detail here and in the next section.

Table II. Computational Details Regarding the Isoprene Transition State Grid Structure

grid characteristic	value
total number of grid points	232897
spatial spread of the grid along donor/acceptor direction	1.2 Å
spatial spread of the grid in orthogonal directions	0.5 Å
grid spacing along donor/acceptor direction	0.012 Å
grid spacing along directions orthogonal to the donor/acceptor direction	0.010 Å
number of grid points along donor/acceptor	97
number of grid points along orthogonal directions	49
levels of theory used in computing the surface	B3LYP/6-311++g(d,p) M062x/6-311++g(d,p)
average number of sample points[a] obtained from tessellation of ω_S	373 (B3LYP) 367(M062x)
data compression rate, that is reduction	0.16% (B3LYP)
in number of electronic structure calculations	0.15%

[a]Per iteration and for each point along the reaction coordinate.

Table III. Transmission Amplitudes Computed at Each Transition State Using the Potential Surfaces Computed[b]

transition state	theory	amplitude (%)	ZPE[a] (kcal/mol)
1	B3LYP/6-311++g(d,p)	97	7.93
	M062x/6-311++g(d,p)	99	8.35
2	B3LYP/6-311++g(d,p)	84	8.29
	M062x/6-311++g(d,p)	97	9.45
3	B3LYP/6-311++g(d,p)	72	7.93
	M062x/6-311++g(d,p)	86	8.80
4	B3LYP/6-311++g(d,p)	95	7.91
	M062x/6-311++g(d,p)	98	8.60
5	B3LYP/6-311++g(d,p)	61	7.55
	M062x/6-311++g(d,p)	77	9.29

[a]For the 3D potential. [b]The zero-point energy corresponding to each surface is also noted.

The hydrogen nuclear ground eigenstates, for the B3LYP surfaces, are shown in Figure 11. For transition states 1, 2, and 4 the ground eigenstate populates the product well to a large extent. This is seen from the transition probabilities noted in Table III where the corresponding values for transition states 1 and 4 are 97% and 95%, respectively. To further gauge this effect of enhanced product-side populations at the transition state geometries, in Figure 11, we present two-dimensional slices of the potential that include the global minimum for each potential surface. While the double-well nature of each potential is evident, there are subtle differences that directly address the product side delocalization and associated transmission probabilities reported in Table III. For example, for transitions states 1 and 4, the acceptor side well is deeper than the donor side well, which explains the transmission probabilities in these cases. For transition states 3 and 5, the reactant and product side wells are closer to each other, and this aspect results in a greater delocalization of the ground state wavepacket on either sides of the barrier as is clearly visible from Figure 11(c) and 11(h). The smaller difference in energy between the two minima in transition state 2 is also countered by the larger barrier and larger separation between the two minima. However, the fact that the two minima are closer in
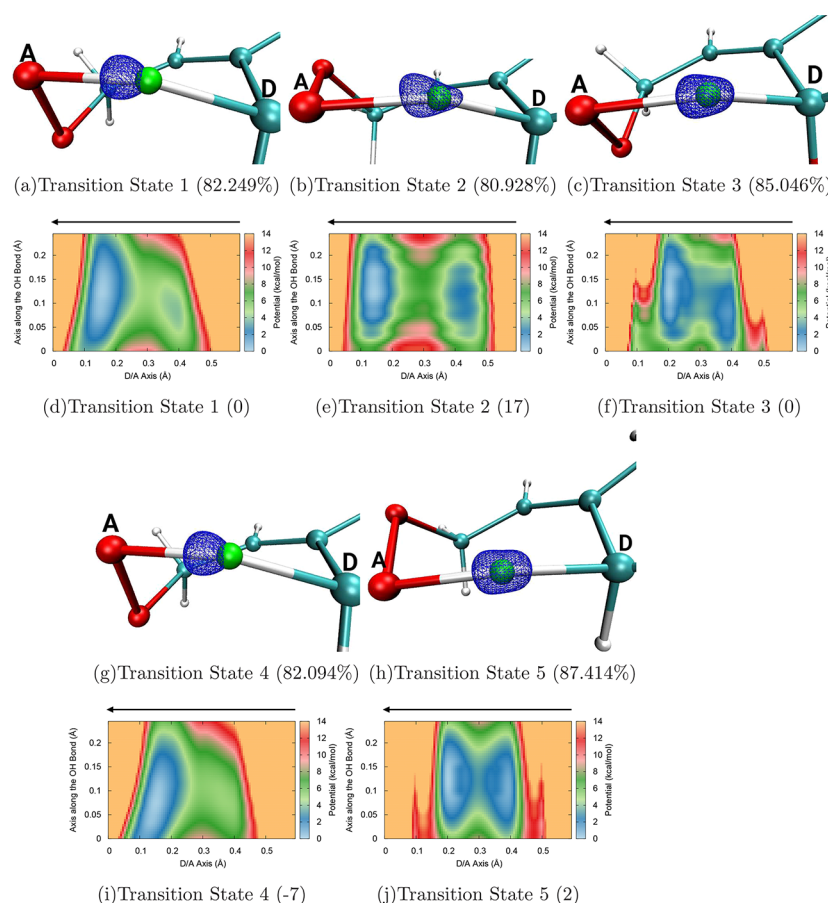
(a)Transition State 1 (82.249%) (b)Transition State 2 (80.928%) (c)Transition State 3 (85.046%)

(d)Transition State 1 (0) (e)Transition State 2 (17) (f)Transition State 3 (0)

(g)Transition State 4 (82.094%) (h)Transition State 5 (87.414%)

(i)Transition State 4 (-7) (j)Transition State 5 (2)

Figure 11. Hydrogen ground eigenstates for all five of the transition states are shown using blue mesh diagrams superimposed on top of the TS structures (enclosed probability listed in the subfigure caption). The green solid spheres are the classical hydrogen nuclear positions. The contour diagrams shown below each structure represent a cross section of the potential surface [B3LYP/6-311++g(d,p)] at the slice that contains the global minimum.
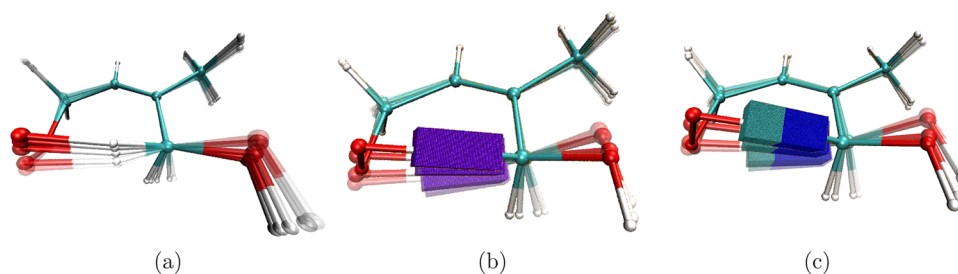

(a)   (b)   (c)

Figure 12. Evolution of geometries of transition state 1 along the hydrogen nuclear-transfer coordinate. The more opaque geometries are closer to the transition state. Here (a) shows geometries along the hydrogen-transfer coordinate, (b) shows the body-fixed reference frame for quantum nuclear degrees of freedom, and (c) shows the basis to compute the transmission amplitudes. Here the light blue points represent the domain of product state basis functions used to compute the transmission amplitudes.

energy (as compared to transition states 1 and 4) is responsible for the bimodal form of the ground eigenstate in Figure 11(b).

Given the anomalous product side transmission at this transition state geometry, in the next subsection we inspect the evolution of ground eigenstates along a hydrogen-transfer reaction coordinate for transition state 1. However, the power of the recursive refinement algorithm when used in conjunction with ω_S and ω_ρ, and the accompanying tiling mechanism, is already clear, with reference to the solution to such complex kinetics problems that involve hydrogen-transfer processes.

III.C. Evolution of the Hydrogen Nuclear Transmission along an Effective Reaction Coordinate. Due to the fact

that there is significant transmission noted in Section III.B prior to the classical transition state, we expect that the quantum nuclear eigenstate energy corrected transition state for the hydrogen-transfer step would appear closer to the reactant. Similar results have been noted for the enzyme soybean lipoxygenase-1 in ref 35. To further gauge the problem here, we consider the evolution of hydrogen and deuterium nuclear ground state wave functions as a function of a hydrogen-transfer coordinate. The geometries along such a hydrogen-transfer reaction coordinate were obtained through a sequence of relaxed scan calculations where the donor-transferring-hydrogen distance was sequentially incremented. Figure 12

shows the geometries encountered along this (intrinsic reaction coordinate or) transfer coordinate for transition state 1. All geometries were obtained at the B3LYP/6-311++g(d,p) level of theory, and we used 48 geometries, incrementally placed, along the reaction pathway. Recursive refinement was used to compute potential surfaces and eigenstates for hydrogen and deuterium nuclear-transfer processes along the aforementioned reaction coordinate. For each geometry, along the reaction coordinate, a body-fixed reference frame was used to provide the coordinate representation for the quantum nuclear dimensions. The associated quantum nuclear grid basis was defined using (a) the donor−acceptor axis, (b) an orthogonal axis directed along the plane defined by the donor−acceptor axis and the CO bond, and (c) a direction axis orthogonal to the two degrees of freedom mentioned above. The evolution of such a body-fixed reference frame along the reaction coordinate is shown in Figure 12(b) for transition state 1. To compute the transmission amplitude along this reaction coordinate, we generated a series of product-state basis functions that are shown in Figure 12(c). To generate these functions, we first compute the ratio between the donor/transferring-hydrogen distance and the donor/acceptor distance for each grid point. When this ratio is greater that the corresponding value for the classical transition state, the grid point is deemed to reside on the product side. The set of all points on the product side then forms the product side basis function, and the dependence of these basis functions, along the reaction coordinate, is shown in Figure 12(c).

The transmission of the hydrogen and deuterium ground states was then computed as the inner product of the ground state with the product side basis functions discussed above. The evolution of these quantities is shown in Figure 13, and the
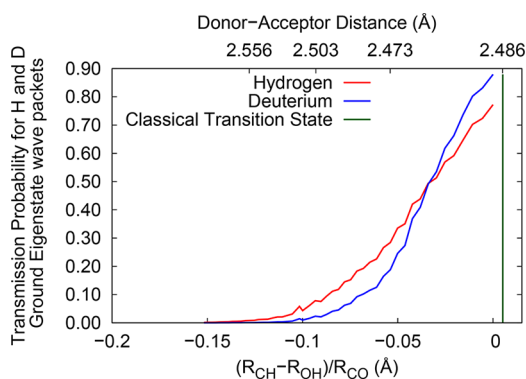
corresponding reaction coordinate dependent eigenstates are shown in Figure 14. The transmission of ground state probability, prior to the classical transition state, depicted in Figure 13 is also seen from the product side delocalization of the eigenstates in Figure 14. Future publications will gauge the effect of this early product-side delocalization on the rate constant for the reaction. It is, however, abundantly clear that the recursive refinement procedure introduced here is capable of addressing these complex multidimensional hydrogen-transfer problems at reduced computational costs.

IV. CONCLUSIONS

In this publication we have discussed the use of two different sampling functions (eqs 3 and 4) to gauge significant areas of a potential energy surface. These sampling functions depend on the wave function, potential, its gradients, and the local Shannon entropy associated with the potential. These sampling functions are shown to provide good estimates of the local-Nyquist frequency of the potential, and this aspect is numerically tested. Thus, the goal here is to appropriately and adaptively adjust the sampling rate of the potential based on local "ruggedness" as defined by the local variations in the Nyquist frequency. The sampling rates afforded by the introduction of these sampling functions (eqs 3 and 4) are then constructed through a multidimensional tessellation or meshing algorithm, and here we have presented both rectangular meshing and a brief description of irregular meshing through the use of Voronoi diagrams. The procedure is then used within a recursive refinement procedure to self-consistently improve the accuracy of a potential surface. Different fitting procedures are tested in conjunction with the sampling procedure and lead to an overall reduction in the number of electronic structure calculations required, by several orders of magnitude, to obtain the potential surface.

Numerical tests are conducted for (a) the highly anharmonic potential surface associated with the shared proton in a bihalide XHX^{-1} system and (b) for a more complex hydrogen-transfer reaction that appears during the oxidation of a biogenic volatile organic compound, isoprene. In the case of XHX^-, the recursive refinement procedure coupled with the sampling functions discussed above provides an efficient and accurate method for potential surfaces calculations. For the isoprene problem, we have probed the quantum nuclear effects emanating from the transferring H/D-dimensions and find that there is substantial probability accumulating on the product side prior to arrival at the classical transition state. While this picture is currently adiabatic, future publications will gauge the use of the sampling procedure to accurately compute rates in such hydrogen-transfer reactions by engaging the fully

Figure 13. Transmission of the ground eigenstate for hydrogen and deuterium into the product well for the transition state labeled 1 in Figure 7.

(a)**80%** (-0.113 Å)   (b)**76%** (-0.081 Å)   (c)**74%** (-0.046 Å)   (d)**75%** (0.000 Å)
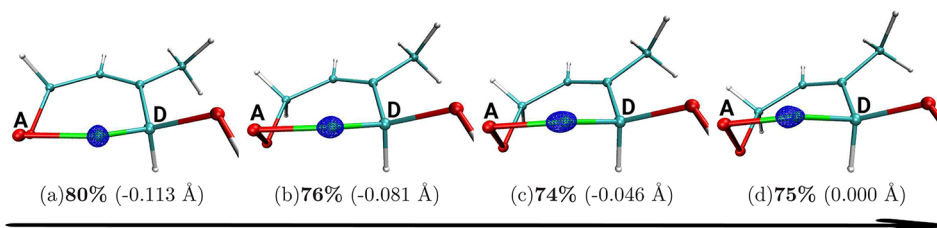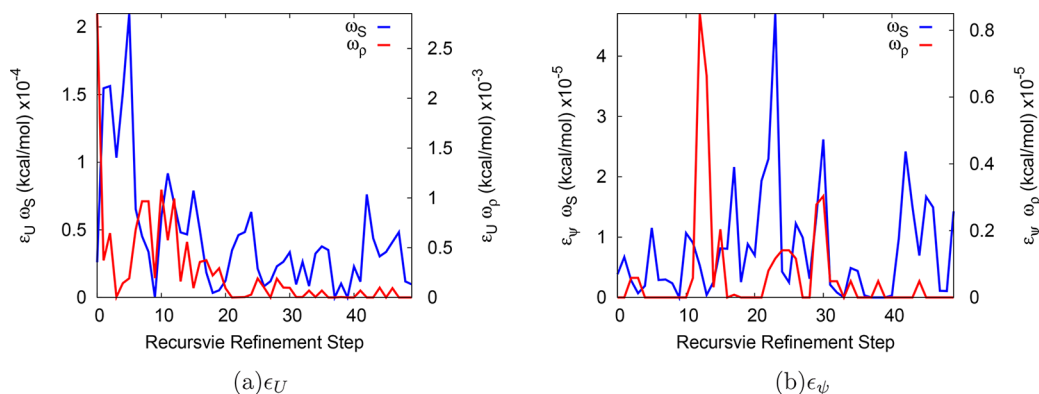
Figure 14. Hydrogen nuclear ground eigenstates along the transfer coordinate for transition state 1. The enclosed probability in each case is shown in the figure caption, and numbers in parentheses indicate the values of the reaction coordinate (horizontal axis in Figure 13). The classical position for the transferring hydrogen nucleus is shown in green. The arrow is directed from the reactant configuration toward the classical transition state with part (d) being the closest to the transition state.

Figure 15. Change in potential between consecutive recursive refinement steps. Based on eqs B1 and eq B2.

nonadiabatic nature of interactions between the reaction coordinates and the transferring H/D-dimensions, including associated quantum nuclear effects, such as tunneling.

In conclusion recursive refinement coupled with the sampling functions, ω_S and ω_ρ, provide accurate potential energy surfaces with a large increase in computational efficiency. This is done by adaptively sampling critical regions of the potential.

■ APPENDIX A: INTERPOLATION METHODS USED IN THIS WORK

As stated before, multiple methods have been employed here to obtain the potential energy fits. All interpolation schemes are standard protocols available in the literature. The relevant parameters and other details about the interpolation procedures used in this work are discussed below.

1. In one approach a locally independent Hermite curve interpolation (referenced as local-Hermite in further discussion) is constructed inside each *tile* or Nyquist domain, and this provides a potential surface at all grid points. In essence this reduces the full potential into a piece-wise smooth, continuous, and differential local spline fit, where locality is defined by the tile-size (or sample rate) obtained from the sampling functions.

2. A second approach we benchmark here is the well-known permutationally invariant polynomials introduced by Bowman and co-workers.[19,21−24] Here monomial symmetrization (MSA) is used to construct monomials that are invariant under permutation of all like-atoms. These have been well-benchmarked[19,21−24] and have been used to compute full global potentials in many complex systems with multiple (up to 27) degrees of freedom. Here we employ MSA to compute the reduced dimensional potentials for hydrogen-bonded systems and hydrogen-transfer reaction as detailed in the main body of the paper. All instances of MSA used order-4 polynomials to fit the surfaces. This choice was based on independent numerical tests on double-well potentials that gauged the accuracy and efficiency of MSA over the polynomial range 1 through 12.

3. A third set of fitting functions that we benchmark here is a low-pass (Gaussian) filtered version of the Lagrange interpolation function[34,152]

$$f(\overline{x}) = \sum_j \left\{ \mathcal{G}(\overline{x} - \overline{x}_j; \sigma) \prod_\alpha^{N_{Dim}} \left[\prod_{x_i^\alpha \neq x_j^\alpha} \Theta(\sigma' - |\overline{x} - \overline{x}_i|) \frac{x^\alpha - x_i^\alpha}{x_j^\alpha - x_i^\alpha} \right] \right\} f(\overline{x}_j) \tag{A1}$$

where $\mathcal{G}(\overline{x} - \overline{x}_j; \sigma)$ is a multidimensional Gaussian function, and, for example, x_i^α represents the α-th component of grid point i. That is, $\overline{x} \equiv \{x^1, x^2, \cdots, x^\alpha, \cdots, x^{N_{Dim}}\}$. The quantity $\Theta(\sigma' - |\overline{x} - \overline{x}_i|)$ represents a step function that is equal to 1 when grid point $\overline{x}_i$ is less than a distance σ' from $\overline{x}$. Based on several numerical tests, here σ is chosen to be 0.22, and σ' is chosen to be 0.106 Å. This modification to Lagrange interpolation is constructed to reduce the well-known Runge oscillation problem[150] (or the Gibbs phenomenon) in standard Lagrange interpolation, and the choice of values above is obtained by studying the behavior of the fit for a range of values for these variables for a double potential. Here, this fitting function is denoted as Lagrange-Low-pass filter (Lag-LPF). These are closely related to the Lagrange-Distributed approximating functionals[152,153] introduced by Kouri and co-workers.

4. Finally, we have also used both Shepard interpolation[154] (inverse distance weighted with power of dimensionality plus one) and a modified version of Shepard interpolation that employs a local first-order Taylor expansion about each sampled grid point[155]

$$f(\overline{x}) = \sum_i^N \left\{ \frac{\|x - x_i\|^{-p}}{\sum_k^N \|x - x_k\|^{-p}} \tilde{f}(\overline{x}_i) \right\} \tag{A2}$$

where N defines a local subset of sampling points determined by the distance between $\overline{x}$ and $\overline{x}_i$. The quantity $\|\cdots\|^{-p}$ is the Euclidean distance with power $p = N_{Dim}+1$, and $\tilde{f}(\overline{x}_i)$ is the potential, in the case of Shepard interpolation, and first order Taylor expansion of the potential in the case of the modified Shepard algorithm.

It is useful to discuss the connections between local-Hermite, MSA, and low-pass filtered version of the Lagrange interpolation. The MSA methodology represents the potential as a linear combination of monomial functions written in terms of interatomic distance variables. Furthermore, when the permutation symmetry of the potential associated with like-nuclear position exchange is used, the number of monomial coefficients can be significantly reduced in most cases. Here, we have used the idea of monomial expansions in Cartesian coordinates pertaining to the reduced dimensional degrees of freedom explained in the paper, but without symmetry, and have used the infrastructure already present in the MSA computer program[21] to carry out these calculations.

Furthermore, we note that eq A1 may also be interpreted as a linear combination of monomials; however, these monomials are (i) centered on the sample points, $\{x_i\}$, and (ii) their spacial extents are damped by the low-pass filter and the step functions
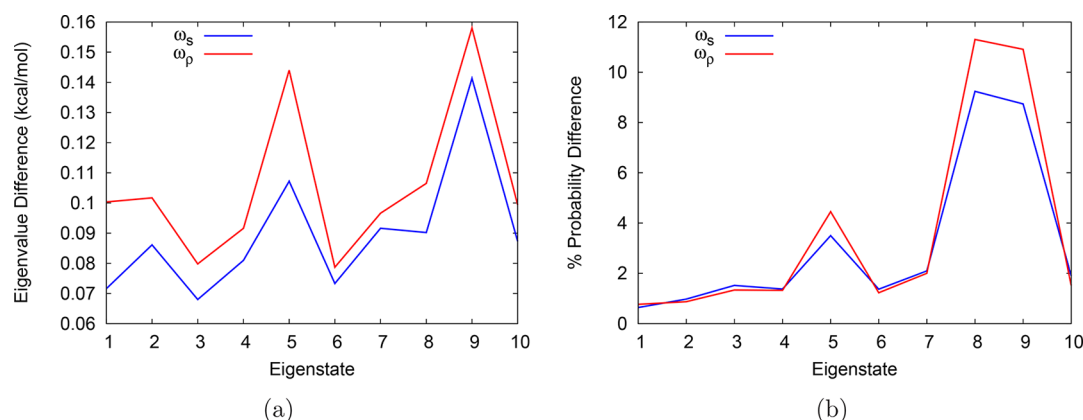
Figure 16. Accuracy of eigenvalues [part (a)] and eigenstates, $\Delta\rho_i$ in eq B3 [part (b)], obtained through the recursively refined directed measure algorithm presented here.

in eq A1. The local-Hermite approximation, on the contrary, is a local monomial expansion of order 3. Here, the word "local" is to be interpreted as being inside a certain tessellation region or a *tile*. The local-Hermite approximation uses potentials and gradients available from electronic structure calculations performed on the sampled set of grid points.

In this publication we use all four methods and compare their accuracies in computing surfaces obtained from the local sampling estimates provided by eqs 3 and 4. It is, however, critical to note that these procedures are independent of our sampling scheme that generates points on the surface in an adaptive fashion.

■ APPENDIX B: CONVERGENCE OF THE RECURSIVE REFINEMENT FORMALISM AND ASSOCIATED COMPUTATIONAL GAIN FROM USING ω_S AND ω_ρ TO TARGET THE POTENTIAL ENERGY CALCULATIONS

To evaluate the convergence of the recursive refinement method described in Section II, interpolated surfaces for
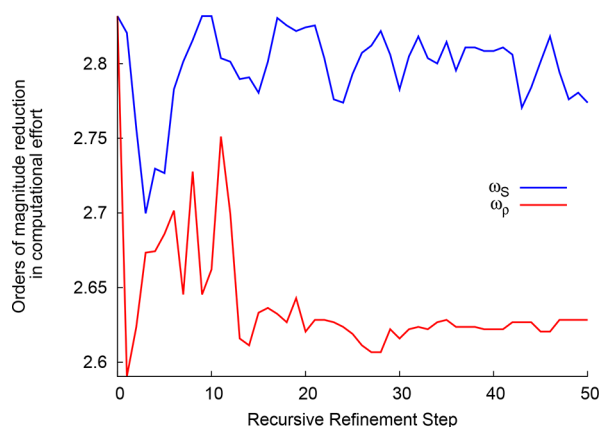

Figure 17. Overall efficiency of the geometric tessellation based recursive refinement methodology with the drastic (nearly 3 orders of magnitude) reduction in number of electronic structure calculations. These translate to an equivalent computational gain.

transition states marked as "1" in Figure 7 were compared with the full surface obtained from the PM6 level of theory. The associated grid over which the shared hydrogen is quantized is shown in Figure 8 and uses the same specifications in Table II.

Table IV. Average Order of Reduction over 51 Recursive Refinement Steps

transition state	level of theory	ω_S,[a] convergence[b]	ω_ρ,[a] convergence[b]
1	B3LYP/6-311++g(d,p)	2.8 (0.004)	2.6 (0.007)
	M062x/6-311++g(d,p)	2.8 (0.004)	1.6 (0.012)
2	B3LYP/6-311++g(d,p)	2.7 (0.006)	2.7 (0.004)
	M062x/6-311++g(d,p)	2.7 (0.005)	2.7 (0.005)
3	B3LYP/6-311++g(d,p)	2.7 (0.034)	2.8 (0.007)
	M062x/6-311++g(d,p)	2.7 (0.036)	2.7 (0.011)
4	B3LYP/6-311++g(d,p)	2.8 (0.003)	2.6 (0.006)
	M062x/6-311++g(d,p)	2.8 (0.003)	2.6 (0.004)
5	B3LYP/6-311++g(d,p)	2.7 (0.029)	2.8 (0.281)[c]
	M062x/6-311++g(d,p)	2.7 (0.038)	2.7 (0.984)[c]

[a]$\log\left(\frac{N}{P}\right)$ where N is the total number of grid points, and P is the prescribed number of sampling points. Thus, $\log\left(\frac{N}{P}\right)$ represents the order of magnitude of grid compression facilitated through the use of ω_S and ω_ρ. [b]RMS deviation in eq B1, over the last 21 recursive refinement cycles. [c]These energies large changes are due to fluctuations in the high energy regions.

The recursive refinement process on the Boxcar tessellated grids was performed for 51 cycles for the sampling functions in eqs 3 and 4. To gauge the convergence of the recursive technique, we compute errors similar to eqs 9 and 10 but across recursive refinement steps as

$$\epsilon_U = \frac{1}{N} \sum_i |V_F(\bar{x}_i) - V_{F-1}(\bar{x}_i)| \tag{B1}$$

$$\epsilon_\psi = \sum_i |\psi_0(\bar{x}_i)|^2 \times |V_F(\bar{x}_i) - V_{F-1}(\bar{x}_i)| \tag{B2}$$

where F is the index that represent the refinement step, N is the total number of grid points, and $\psi_0(\bar{x}_i)$ is the ground eigenstate. The resulting analysis is presented in Figure 15. Overall as seen in Figure 15(a), ω_S converges much faster than ω_ρ. Both sampling functions converge to extremely high precision.

To further gauge the accuracy of the potential obtained after convergence, we compute the first few eigenvalues and eigenfunctions for each converged potential and compare it with those obtained from the full PM6 grid calculation. Figure 16(a) shows the error in the first 10 eigenvalues thus obtained. While both sampling functions appear to be quite adequate, ω_S clearly is slightly better as seen in the eigenvalues in Figure

16(a). In Figure 16(b) the accuracy of the ith eigenstate probabilities is shown using

$$\Delta\rho_i = \left[\int d\overline{x}|(\Psi_i(\overline{x})_{\text{int}})^2 - (\Psi_i(\overline{x})_{\text{full}})^2|\right] \times 100 \tag{B3}$$

It can be seen from Figure 16(b) that the error in the lowest 4 eigenstates is less than 1.6% for both ω_S and ω_ρ. Furthermore, the number of grid points used in these calculations is *nearly 2.8 orders of magnitude smaller than the full grid* as indicated in Figure 17, ω_S being more efficient as compared to ω_ρ. More details regarding scaling and convergence of the recursive refinement process are provided in Table IV.

■ AUTHOR INFORMATION

Corresponding Author
*E-mail: iyengar@indiana.edu.

ORCID ⓘ
Srinivasan S. Iyengar: 0000-0001-6526-2907

■ REFERENCES

(1) *Hydrogen-Transfer Reactions*; Hynes, J. T., Klinman, J. P., Limbach, H.-H., Schowen, R. L., Eds.; Wiley-VCH: Weinheim, Germany, 2007; DOI: 10.1002/9783527611546.

(2) Gertner, B. J.; Hynes, J. T. Molecular Dynamics Simulation of Hydrochloric Acid Ionization at the Surface of Stratospheric Ice. *Science* **1996**, *271*, 1563.

(3) Devlin, J. P.; Uras, N.; Sadlej, J.; Buch, V. Discrete Stages in the Solvation and Ionization of Hydrogen Chloride Adsorbed on Ice Particles. *Nature* **2002**, *417*, 269.

(4) Aloisio, J. S.; Francisco, S. Radical Water Complexes in Earth's Atmosphere. *Acc. Chem. Res.* **2000**, *33*, 825.

(5) Iyengar, S. S. Dynamical Effects on Vibrational and Electronic Spectra of Hydroperoxyl Radical Water Clusters. *J. Chem. Phys.* **2005**, *123*, 084310.

(6) Nagel, Z.; Klinman, J. Tunneling and Dynamics in Enzymatic Hydride Transfer. *Chem. Rev.* **2006**, *106*, 3095.

(7) Cleland, W. W.; Frey, P. A.; Gerlt, J. A. The low barrier hydrogen bond in enzymatic catalysis. *J. Biol. Chem.* **1998**, *273*, 25529−25532.

(8) Warshel, A.; Papazyan, A.; Kollman, P. A. On Low-Barrier Hydrogen-Bonds and Enzyme Catalysis. *Science* **1995**, *269*, 102.

(9) Haile, S. M.; Boysen, D. A.; Chisholm, C. R. I.; Merle, R. B. Solid Acids As Fuel Cell Electrolytes. *Nature* **2001**, *410*, 910.

(10) Schuster, M. F.; Meyer, W. H. Anhydrous Proton-Conducting Polymers. *Annu. Rev. Mater. Res.* **2003**, *33*, 233.

(11) Kreuer, K. D.; Fuchs, A.; Ise, M.; Spaeth, M.; Maier, J. Imidazole and Pyrazole-Based Proton Conducting Polymers and Liquids. *Electrochim. Acta* **1998**, *43*, 1281.

(12) Iannuzzi, M.; Parrinello, M. Proton Transfer in Heterocycle Crystals. *Phys. Rev. Lett.* **2004**, *93*, 025901.

(13) Hudson, B. S.; Verdal, N. Vibrational Dynamics in Short, Strong Symmetric Hydrogen Bonds: General Considerations and Two Examples. *Phys. B* **2006**, *385-386*, 212.

(14) Murrell, J.; Carter, S.; Farantos, S.; Huxley, P.; Varandas, A. *Molecular Potential Energy Functions*; Wiley: New York, 1984.

(15) Truhlar, D.; Hase, W.; Hynes, J. *J. Phys. Chem.* **1983**, *87*, 2664.

(16) Xie, Z.; Bowman, J. M. Permutationally Invariant Polynomial Basis for Molecular Energy Surface Fitting Via Monomial Symmetrization. *J. Chem. Theory Comput.* **2010**, *6*, 26.

(17) Schatz, G. C. The Analytical Representation of Electronic Potential-Energy Surfaces. *Rev. Mod. Phys.* **1989**, *61*, 669.

(18) Hollebeek, T.; Ho, T. S.; Rabitz, H. Constructing Multidimensional Molecular Potential Energy Surfaces from Ab Initio Data. *Annu. Rev. Phys. Chem.* **1999**, *50*, 537.

(19) Braams, B. J.; Bowman, J. M. Permutationally invariant potential energy surfaces in high dimensionality. *Int. Rev. Phys. Chem.* **2009**, *28*, 577.

(20) Dahlke, E. E.; Truhlar, D. G. Electrostatically Embedded Many Body Expansion for Large Systems, with Applications to Water Clusters. *J. Chem. Theory Comput.* **2007**, *3*, 46.

(21) Conte, R.; Qu, C.; Bowman, J. M. Permutationally Invariant Fitting of Many-Body, Non-covalent Interactions with Application to Three-Body Methane-Water-Water. *J. Chem. Theory Comput.* **2015**, *11*, 1631−1638.

(22) Mancini, J. S.; Bowman, J. M. A New Many-Body Potential Energy Surface for HCl Clusters and Its Application to Anharmonic Spectroscopy and Vibration-Vibration Energy Transfer in the HCl Trimer. *J. Phys. Chem. A* **2014**, *118*, 7367−7374.

(23) Wang, Y.; Bowman, J. M.; Kamarchik, E. Five ab initio potential energy and dipole moment surfaces for hydrated NaCl and NaF. I. Two-body interactions. *J. Chem. Phys.* **2016**, *144*, 114311.

(24) Conte, R.; Houston, P. L.; Bowman, J. M. Trajectory and Model Studies of Collisions of Highly Excited Methane with Water Using an ab Initio Potential. *J. Phys. Chem. A* **2015**, *119*, 12304−12317.

(25) Yu, Q.; Bowman, J. M. High-level Quantum Calculations of the IR Spectra of the Eigen, Zundel and Ring Isomers of $H^+(H_2O)_4$. *J. Am. Chem. Soc.* **2017**, *139*, 10984.

(26) Pack, R. T.; Parker, G. A. *J. Chem. Phys.* **1987**, *87*, 3888.

(27) Willow, S. Y.; Salim, M. A.; Kim, K. S.; Hirata, S. Ab initio molecular dynamics of liquid water using embedded fragment second-order many-body perturbation theory towards its accurate property prediction. *Sci. Rep.* **2015**, *5*, 14358.

(28) Saller, M. A. C.; Habershon, S. Basis Set Generation for Quantum Dynamics Simulations Using Simple Trajectory-Based Methods. *J. Chem. Theory Comput.* **2015**, *11*, 8−16.

(29) Reilly, A. M.; Habershon, S.; Morrison, C. A.; Rankin, D. W. H. Determination of the experimental equilibrium structure of solid nitromethane using path-integral molecular dynamics simulations. *J. Chem. Phys.* **2010**, *132*, 094502.

(30) Collins, M. A.; Godsi, O.; Liu, S.; Zhang, D. H. An ab initio quasi-diabatic potential energy matrix for $OH(^2\Sigma)$ + H_2. *J. Chem. Phys.* **2011**, *135*, 234307.

(31) Evenhuis, C. R.; Lin, X.; Zhang, D. H.; Yarkony, D.; Collins, M. A. Interpolation of diabatic potential-energy surfaces: Quantum dynamics on ab initio surfaces. *J. Chem. Phys.* **2005**, *123*, 134110.

(32) Zhou, Y.; Fu, B.; Wang, C.; Collins, M. A.; Zhang, D. H. Ab initio potential energy surface and quantum dynamics for the $H+CH_4 \rightarrow H_2 + CH_3$ reaction. *J. Chem. Phys.* **2011**, *134*, 064323.

(33) Iyengar, S. S.; Jakowski, J. Quantum Wavepacket Ab Initio Molecular Dynamics: An Approach to Study Quantum Dynamics in Large Systems. *J. Chem. Phys.* **2005**, *122*, 114105.

(34) Sumner, I.; Iyengar, S. S. Quantum Wavepacket *Ab Initio* Molecular Dynamics: An Approach for Computing Dynamically Averaged Vibrational Spectra Including Critical Nuclear Quantum Effects. *J. Phys. Chem. A* **2007**, *111*, 10313.

(35) Iyengar, S. S.; Sumner, I.; Jakowski, J. Hydrogen Tunneling in an Enzyme Active Site: A Quantum Wavepacket Dynamical Perspective. *J. Phys. Chem. B* **2008**, *112*, 7601.

(36) Yang, W. Direct Calculation of Electron Density in Density-Functional Theory. *Phys. Rev. Lett.* **1991**, *66*, 1438.

(37) Maseras, F.; Morokuma, K. A New "Ab Initio + Molecular Mechanics" Geometry Optimization Scheme of Equilibrium Structures and Transition States. *J. Comput. Chem.* **1995**, *16*, 1170.

(38) Gordon, M. S.; Freitag, M. A.; Bandyopadhyay, P.; Jensen, J. H.; Kairys, V.; Stevens, W. J. The Effective Fragment Potential Method: A QM-Based MM Approach to Modeling Environmental Effects in Chemistry. *J. Phys. Chem. A* **2001**, *105*, 293.

(39) Gordon, M.; Mullin, J.; Pruitt, S.; Roskop, L.; Slipchenko, L.; Boatz, J. Accurate Methods for Large Molecular Systems. *J. Phys. Chem. B* **2009**, *113*, 9646.

(40) Zhang, D. W.; Zhang, J. Z. H. Molecular Fractionation with Conjugate Caps for Full Quantum Mechanical Calculation of Protein-molecule Interaction Energy. *J. Chem. Phys.* **2003**, *119*, 3599.

(41) Liu, J.; Zhu, T.; Wang, X.; He, X.; Zhang, J. Z. H. Quantum Fragment Based ab Initio Molecular Dynamics for Proteins. *J. Chem. Theory Comput.* **2015**, *11*, 5897.

(42) Dahlke, E. E.; Truhlar, D. G. Electrostatically Embedded Many Body Expansion for Simulations. *J. Chem. Theory Comput.* **2008**, *4*, 1.

(43) Li, S.; Li, W.; Ma, J. Generalized Energy-Based Fragmentation Approach and Its Applications to Macromolecules and Molecular Aggregates. *Acc. Chem. Res.* **2014**, *47*, 2712.

(44) Wang, L.-W.; Zhao, Z.; Meza, J. Linear-Scaling Three-Dimensional Fragment method for Large-scale Electronic Structure Calculations. *Phys. Rev. B: Condens. Matter Mater. Phys.* **2008**, *77*, 165113.

(45) Kerdcharoen, T.; Morokuma, K. ONIOM-XS: An Extension of the ONIOM Method for Molecular Simulation in Condensed Phase. *Chem. Phys. Lett.* **2002**, *355*, 257.

(46) Ganesh, V.; Dongare, R. K.; Balanarayan, P.; Gadre, S. R. Molecular Tailoring Approach for Geometry Optimization of Large Molecules: Energy Evaluation and Parallelization Strategies. *J. Chem. Phys.* **2006**, *125*, 104109.

(47) Guo, W.; Wu, A.; Xu, X. XO: An Extended ONIOM Method for Accurate and Efficient Geometry Optimization of Large Molecules. *Chem. Phys. Lett.* **2010**, *498*, 203−208.

(48) Raghavachari, K.; Saha, A. Accurate Composite and Fragment-Based Quantum Chemical Models for Large Molecules. *Chem. Rev.* **2015**, *115*, 5643.

(49) Mayhall, N. J.; Raghavachari, K. Molecules-In-Molecules: An Extrapolated Fragment-Based Approach for Accurate Calculations on Large Molecules and Materials. *J. Chem. Theory Comput.* **2011**, *7*, 1336.

(50) Mayhall, N. J.; Raghavachari, K. Many-Overlapping-Body (MOB) Expansion: A Generalized Many Body Expansion for Nondisjoint Monomers in Molecular Fragmentation Calculations of Covalent Molecules. *J. Chem. Theory Comput.* **2012**, *8*, 2669.

(51) Jacobson, L. D.; Herbert, J. M. An Efficient, Fragment-Based Electronic Structure Method for Molecular Systems: Self-Consistent Polarization with Perturbative Two-Body Exchange and Dispersion. *J. Chem. Phys.* **2011**, *134*, 094118.

(52) Richard, R. M.; Herbert, J. M. A Generalized Many-Body Expansion and a Unified View of Fragment-Based Methods in Electronic Structure Theory. *J. Chem. Phys.* **2012**, *137*, 064113.

(53) Hirata, S. Fast Electron-Correlation Methods for Molecular Crystals: an Application to the α, $\beta(1)$, and $\beta(2)$ Modifications of Solid Formic Acid. *J. Chem. Phys.* **2008**, *129*, 204104.

(54) Kamiya, M.; Hirata, S.; Valiev, M. Fast Electron-Correlation Methods for Molecular Crystals Without Basis Set Superposition Errors. *J. Chem. Phys.* **2008**, *128*, 074103.

(55) Beran, G. J. O.; Hirata, S. Fragment and Localized Orbital Methods in Electronic Structure Theory. *Phys. Chem. Chem. Phys.* **2012**, *14*, 7559.

(56) Brorsen, K. R.; Minezawa, N.; Xu, F.; Windus, T. L.; Gordon, M. S. Fragment Molecular Orbital Molecular Dynamics with the Fully Analytic Energy Gradient. *J. Chem. Theory Comput.* **2012**, *8*, 5008.

(57) Brorsen, K. R.; Zahariev, F.; Nakata, H.; Fedorov, D. G.; Gordon, M. S. Analytic Gradient for Density Functional Theory Based

on the Fragment Molecular Orbital Method. *J. Chem. Theory Comput.* **2014**, *10*, 5297.

(58) Le, H.-A.; Tan, H.-J.; Ouyang, J. F.; Bettens, R. P. A. Combined Fragmentation Method: A Simple Method for Fragmentation of Large Molecules. *J. Chem. Theory Comput.* **2012**, *8*, 469.

(59) Han, J.; Mazack, M. J. M.; Zhang, P.; Truhlar, D. G.; Gao, J. Quantum Mechanical Force Field for Water with Explicit Electronic Polarization. *J. Chem. Phys.* **2013**, *139*, 054503.

(60) Gordon, M. S.; Fedorov, D. G.; Pruitt, S. R.; Slipchenko, L. V. Fragmentation Methods: A Route to Accurate Calculations on Large Systems. *Chem. Rev.* **2012**, *112*, 632.

(61) Xantheas, S. S. *Ab Initio* Studies of Cyclic Water Clusters $(H_2O)_n$, N = 1−6. II. Analysis of Manybody Interactions. *J. Chem. Phys.* **1994**, *100*, 7523.

(62) Collins, M. A.; Bettens, R. P. A. Energy-Based Molecular Fragmentation Methods. *Chem. Rev.* **2015**, *115*, 5607.

(63) Collins, M. A. Systematic Fragmentation of Large Molecules by Annihilation. *Phys. Chem. Chem. Phys.* **2012**, *14*, 7744.

(64) Lange, A. W.; Voth, G. A. Multi-State Approach to Chemical Reactivity in Fragment Based Quantum Chemistry Calculations. *J. Chem. Theory Comput.* **2013**, *9*, 4018.

(65) Komeiji, Y.; Mochizuki, Y.; Nakano, T. Three-Body Expansion and Generalized Dynamic Fragmentation Improve the Fragment Molecular Orbital-Based Molecular Dynamics (FMO-MD). *Chem. Phys. Lett.* **2010**, *484*, 380.

(66) Sisto, A.; Glowacki, D. R.; Martinez, T. J. Ab Initio Nonadiabatic Dynamics of Multichromophore Complexes: A Scalable Graphical-Processing-Unit-Accelerated Exciton Framework. *Acc. Chem. Res.* **2014**, *47*, 2857.

(67) Li, J.; Iyengar, S. S. Ab initio Molecular Dynamics using Recursive, Spatially Separated, Overlapping Model Subsystems Mixed Within an ONIOM Based Fragmentation Energy Extrapolation Technique. *J. Chem. Theory Comput.* **2015**, *11*, 3978−3991.

(68) Li, J.; Haycraft, C.; Iyengar, S. S. Hybrid extended Lagrangian, post-Hartree-Fock Born-Oppenheimer ab initio molecular dynamics using fragment-based electronic structure. *J. Chem. Theory Comput.* **2016**, *12*, 2493.

(69) Haycraft, C.; Li, J.; Iyengar, S. S. On-the-fly" Ab initio molecular dynamics with coupled cluster accuracy. *J. Chem. Theory Comput.* **2017**, *13*, 1887.

(70) Behler, J. Constructing high-dimensional neural network potentials: A tutorial review. *Int. J. Quantum Chem.* **2015**, *115*, 1032−1050.

(71) Rupp, M. Machine learning for quantum mechanics in a nutshell. *Int. J. Quantum Chem.* **2015**, *115*, 1058−1073.

(72) Botu, V.; Ramprasad, R. Adaptive machine learning framework to accelerate ab initio molecular dynamics. *Int. J. Quantum Chem.* **2015**, *115*, 1074−1083.

(73) Kohonen, T. An introduction to neural computing. *Neural Netw.* **1988**, *1*, 3−16.

(74) Handley, C. M.; Popelier, P. L. A. Potential Energy Surfaces Fitted by Artificial Neural Networks. *J. Phys. Chem. A* **2010**, *114*, 3371−3383.

(75) Manzhos, S.; Dawes, R.; Carrington, T. Neural network-based approaches for building high dimensional and quantum dynamics-friendly potential energy surfaces. *Int. J. Quantum Chem.* **2015**, *115*, 1012.

(76) Kondati Natarajan, S.; Morawietz, T.; Behler, J. Representing the potential-energy surface of protonated water clusters by high-dimensional neural network potentials. *Phys. Chem. Chem. Phys.* **2015**, *17*, 8356−8371.

(77) Behler, J.; Parrinello, M. Generalized Neural-Network Representation of High-Dimensional Potential-Energy Surfaces. *Phys. Rev. Lett.* **2007**, *98*, 146401.

(78) Behler, J. Neural network potential-energy surfaces in chemistry: a tool for large-scale simulations. *Phys. Chem. Chem. Phys.* **2011**, *13*, 17930−17955.

(79) Press, W. H.; Teukolsky, S. A.; Vetterling, W. T.; Flannery, B. P. *Numerical Recipes in C*; Cambridge University Press: New York, 1992.

(80) Aurenhammer, F. Voronoi Diagrams — A survey of a fundamental geometric data structure. *ACM Comput. Survey* **1991**, *23*, 345.

(81) Okabe, A.; Boots, B.; Sugihara, K.; Chiu, S. N. *Spatial Tessellations — Concepts and applications of Voronoi diagrams*; John Wiley and Sons: 2000.

(82) Jakowski, J.; Sumner, I.; Iyengar, S. S. Computational Improvements to Quantum Wavepacket Ab Initio Molecular Dynamics Using a Potential-Adapted, Time-Dependent Deterministic Sampling Technique. *J. Chem. Theory Comput.* **2006**, *2*, 1203.

(83) Coffey, T. M.; Wyatt, R. E.; Schieve, W. C. Reconstruction of the Time-Dependent Wave Function Exclusively from Position Data. *Phys. Rev. Lett.* **2011**, *107*, 230403.

(84) Isaacs, N. *Physical Organic Chemistry*; Longman Scientific and Technical; Essex, 1995.

(85) Sheridan, R. Quantum Mechanical Tunneling in Organic Reactive Intermediates. In *Reviews of Reactive Intermediate Chemistry*; Platz, M., Moss, R. A., Maitland Jones, J., Eds.; Wiley-Interscience: Hoboken, NJ, 2007; DOI: 10.1002/9780470120828.ch10.

(86) Hammes-Schiffer, S.; Benkovic, S. J. Relating Protein Motion to Catalysis. *Annu. Rev. Biochem.* **2006**, *75*, 519.

(87) Benkovic, S. J.; Hammes-Schiffer, S. Biochemistry - Enzyme Motions Inside and Out. *Science* **2006**, *312*, 208.

(88) Bahnson, B. J.; Colby, T. D.; Chin, J. K.; Goldstein, B. M.; Klinman, J. P. A Link Between Protein Structure and Enzyme Catalyzed Hydrogen Tunneling. *Proc. Natl. Acad. Sci. U. S. A.* **1997**, *94*, 12797.

(89) Garcia-Viloca, M.; Gao, J.; Karplus, M.; Truhlar, D. G. How Enzymes Work: Analysis by Modern Rate Theory and Computer Simulations. *Science* **2004**, *303*, 186−195.

(90) Olsson, M. H. M.; Siegbahn, P. E. M.; Warshel, A. Simulations of the Large Kinetic Isotope Effect and the Temperature0 Dependence of the Hydrogen Atom Transfer in Lipoxygenase. *J. Am. Chem. Soc.* **2004**, *126*, 2820.

(91) Klinman, J. P. Dynamic Barriers and Tunneling. New Views of Hydrogen Transfer in Enzyme Reactions. *Pure Appl. Chem.* **2003**, *75*, 601.

(92) Liang, Z. X.; Klinman, J. P. Structural Bases of Hydrogen Tunneling in Enzymes: Progress and Puzzles. *Curr. Opin. Struct. Biol.* **2004**, *14*, 648.

(93) Pu, J. Z.; Gao, J. L.; Truhlar, D. G. Multidimensional Tunneling, Recrossing, and the Transmission Coefficient for Enzymatic Reactions. *Chem. Rev.* **2006**, *106*, 3140.

(94) Gao, J. L.; Ma, S. H.; Major, D. T.; Nam, K.; Pu, J. Z.; Truhlar, D. G. Mechanisms and Free Energies of Enzymatic Reactions. *Chem. Rev.* **2006**, *106*, 3188.

(95) Kamerlin, S.; Mavri, J.; Warshel, A. Examining the Case for the Effect of Barrier Compression on Tunneling, Vibrationally Enhanced Catalysis, Catalytic Entropy and Related Issues. *FEBS Lett.* **2010**, *584*, 2759.

(96) Glickman, M. H.; Wiseman, J. S.; Klinman, J. P. Extremely Large Isotope Effects in the Soybean Lipoxygenase-Linoleic Acid Reaction. *J. Am. Chem. Soc.* **1994**, *116*, 793.

(97) Jonsson, T.; Glickman, M. H.; Sun, S. J.; Klinman, J. P. Experimental Evidence for Extensive Tunneling of Hydrogen in the Lipoxygenase Reaction: Implications for Enzyme Catalysis. *J. Am. Chem. Soc.* **1996**, *118*, 10319.

(98) Lehnert, N.; Solomon, E. I. Density-Functional Investigation on the Mechanism of Hatom Abstraction by Lipoxygenase. *J. Biol. Inorg. Chem.* **2003**, *8*, 294.

(99) Hatcher, E.; Soudackov, A. V.; Hammes-Schiffer, S. Proton-Coupled Electron Transfer in Soybean Lipoxygenase. *J. Am. Chem. Soc.* **2004**, *126*, 5763.

(100) Olsson, M. H. M.; Siegbahn, P. E. M.; Warshel, A. Density-Functional Investigation on the Mechanism of Hatom Abstraction by Lipoxygenase. *JBIC, J. Biol. Inorg. Chem.* **2004**, *9*, 96.

(101) Mavri, J.; Liu, H.; Olsson, M. H. M.; Warshel, A. Simulation of Tunneling in Enzyme Catalysis by Combining a Biased Propagation

Approach and the Quantum Classical Path Method: Application to Lipoxygenase. *J. Phys. Chem. B* **2008**, *112*, 5950.

(102) Kohen, A.; Klinman, J. P. Enzyme Catalysis: Beyond Classical Paradigms. *Acc. Chem. Res.* **1998**, *31*, 397.

(103) Rickert, K.; Klinman, J. P. The Nature of Hydrogen Transfer in Soybean Lipoxygenase. *Faseb Journal* **1999**, *13 Suppl. S*, A1529.

(104) Antoniou, D.; Schwartz, S. D. Large Kinetic Isotope Effects in Enzymatic Proton Transfer and the Role of Substrate Oscillations. *Proc. Natl. Acad. Sci. U. S. A.* **1997**, *94*, 12360.

(105) Hatcher, E.; Soudackov, A. V.; Hammes-Schiffer, S. Proton-Coupled Electron Transfer in Soybean Lipoxygenase: Dynamical Behavior and Temperature Dependence of Kinetic Isotope Effects. *J. Am. Chem. Soc.* **2007**, *129*, 187.

(106) Sumner, I.; Iyengar, S. S. Analysis of Hydrogen Tunneling in an Enzyme Active Site Using Von Neumann Measurements. *J. Chem. Theory Comput.* **2010**, *6*, 1698.

(107) Phatak, P.; Sumner, I.; Iyengar, S. S. Gauging the Flexibility of the Active Site in Soybean Lipoxygenase-1 (SLO-1) Through an Atom-Centered Density Matrix Propagation (ADMP) Treatment That Facilitates the Sampling of Rare Events. *J. Phys. Chem. B* **2012**, *116*, 10145.

(108) Phatak, P.; Venderley, J.; Debrota, J.; Li, J.; Iyengar, S. S. Active Site Dynamical Effects That Facilitate the Hydrogen Transfer Process in Soybean Lipoxygenase-1 (SLO-1): Isotope Effects. *J. Phys. Chem. B* **2015**, *119*, 9532.

(109) Rickert, K. W.; Klinman, J. P. Nature of Hydrogen Transfer in Soybean Lipoxygenase 1: Separation of Primary and Secondary Isotope Effects. *Biochemistry* **1999**, *38*, 12218.

(110) Rucker, J.; Klinman, J. P. Computational Study of Tunneling and Coupled Motion in Alcohol Dehydrogenase-Catalyzed Reactions: Implication for Measured Hydrogen and Carbon Isotope Effects. *J. Am. Chem. Soc.* **1999**, *121*, 1997.

(111) Li, X.; Moore, D. T.; Iyengar, S. S. Insights from First Principles Molecular Dynamics Studies Towards Infra-Red Multiple-Photon and Single-Photon Action Spectroscopy: Case Study of the Proton-Bound Di-Methyl Ether Dimer. *J. Chem. Phys.* **2008**, *128*, 184308.

(112) Li, X.; Oomens, J.; Eyler, J. R.; Moore, D. T.; Iyengar, S. S. Isotope Dependent, Temperature Regulated, Energy Repartitioning in a Low-Barrier, Short-Strong Hydrogen Bonded Cluster. *J. Chem. Phys.* **2010**, *132*, 244301.

(113) Dietrick, S. M.; Iyengar, S. S. Constructing Periodic Phase Space Orbits from Ab Initio Molecular Dynamics Trajectories to Analyze Vibrational Spectra: Case Study of the Zundel ($H_5O_2^+$) Cation. *J. Chem. Theory Comput.* **2012**, *8*, 4876.

(114) Peeters, J.; Nguyen, T. L.; Vereecken, L. HOx Radical Regeneration in the Oxidation of Isoprene. *Phys. Chem. Chem. Phys.* **2009**, *11*, 5935.

(115) Nguyen, T. L.; Vereecken, L.; Peeters, J. HO_x Regeneration in the Oxidation of Isoprene III: Theoretical Study of the Key Isomerisation of the Z-δ-Hydroxy-Peroxy Isoprene Radicals. *ChemPhysChem* **2010**, *11*, 3996.

(116) Peeters, J.; Müller, J.-F. M.; Stavrakou, T.; Nguyen, V. S. Hydroxyl Radical Recycling in Isoprene Oxidation Driven by Hydrogen Bonding and Hydrogen Tunneling: The Upgraded LIM1Mechanism. *J. Phys. Chem. A* **2014**, *118*, 8625.

(117) Tan, D.; Faloona, I.; Simpas, J. B.; Brune, W.; Shepson, P. B.; Couch, T. L.; Sumner, A. L.; Carroll, M. A.; Thornberry, T.; Apel, E.; Riemer, D.; Stockwell, W. HO_x Budgets in a Deciduous Forest: Results from the PROPHET Summer 1998 Campaign. *J. Geophys. Res. Atmos.* **2001**, *106*, 24407.

(118) Carslaw, N.; Creasey, D. J.; Harrison, D.; Heard, D. E.; Hunter, M. C.; Jacobs, P. J.; Jenkin, M. E.; Lee, J. D.; Lewis, A. C.; Pilling, M. J.; Saunders, S. M.; Seakins, P. W. OH and HO2 Radical Chemistry in a Forested Region of North-Western Greece. *Atmos. Environ.* **2001**, *35*, 4725.

(119) Lelieveld, J.; Butler, T. M.; Crowley, J. N.; Dillon, T. J.; Fischer, H.; Ganzeveld, L.; Harder, H.; Lawrence, M. G.; Martinez, M.;

Taraborrelli, D.; Williams, J. Atmospheric Oxidation Capacity Sustained by a Tropical Forest. *Nature* **2008**, *452*, 737.

(120) Guenther, A. Atmospheric Chemistry: Are Plant Emissions Green? *Nature* **2008**, *452*, 701.

(121) Martinez, M.; Harder, H.; Kubistin, D.; Rudolf, M.; Bozem, H.; Eerdekens, G.; Fischer, H.; Kluepfel, T.; Gurk, C.; Koenigstedt, R.; Parchatka, U.; Schiller, C. L.; Stickler, A.; Williams, J.; Lelieveld, J. Hydroxyl radicals in the tropical troposphere over the Suriname rainforest: air-borne measurements. *Atmos. Chem. Phys.* **2010**, *10*, 3759−3773.

(122) Swalina, C.; Hammes-Schiffer, S. Impact of Nuclear Quantum Effects on the Molecular Structure of Bihalides and the Hydrogen Fluoride Dimer. *J. Phys. Chem. A* **2005**, *109*, 10410.

(123) Swalina, C.; Pak, M. V.; Hammes-Schiffer, S. Alternative Formulation of Many-Body Perturbation Theory for Electron-Proton Correlation. *Chem. Phys. Lett.* **2005**, *404*, 394.

(124) Li, J.; Li, X.; Iyengar, S. S. Vibrational Properties of Hydrogen Bonded Systems Using the Multi-Reference Generalization to the "On-The-Fly" Electronic Structure Within Quantum Wavepacket *Ab Initio* Molecular Dynamics (QWAIMD). *J. Chem. Theory Comput.* **2014**, *10*, 2265.

(125) Shannon, C. A Mathematical Theory of Communication. *Bell System Technical Journal* **1948**, *27*, 279.

(126) Shannon, C. Communication in the Presence of Noise. *Proc. IEEE* **1998**, *86*, 447.

(127) Sorensen, D. C. Implicit Application of Polynomial Filters in a K-Step Arnoldi Method. *SIAM J. Matr. Anal. Apps.* **1992**, *13*, 357.

(128) Parlett, B. N.; Saad, Y. Complex Shift and Invert Strategies for Real Matrices. *Linear Algebra and its Applications* **1987**, *88-89*, 575.

(129) Golub, G. H.; Loan, C. F. V. *Matrix Computations*; The Johns Hopkins University Press: Baltimore, 1996.

(130) Varga, R. S. *Matrix Iterative Analysis*; Prentice Hall: Englewood Cliffs, NJ, 1963.

(131) Hocker, D.; Li, X.; Iyengar, S. S. Shannon Information Entropy Based Time-Dependent Deterministic Sampling Techniques for Efficient "on-The-Fly" Quantum Dynamics and Electronic Structure. *J. Chem. Theory Comput.* **2011**, *7*, 256.

(132) Wehrl, A. General Properties of Entropy. *Rev. Mod. Phys.* **1978**, *50*, 221.

(133) Sakurai, J. J. *Modern Quantum Mechanics*; Addison-Wesley Publishing Company, 1994.

(134) Madelung, E. Quantentheorie in Hydrodynamischer Form. *Eur. Phys. J. A* **1927**, *40*, 322.

(135) de Broglie, L. *An Introduction to the Study of Wave Mechanics*; E. P. Dutton and Company, Inc.: New York, 1930.

(136) Bohm, D. *Quantum Theory*; Prentice-Hall Inc.: New York, 1951; p 611.

(137) Bohm, D. A Suggested Interpretation of the Quantum Theory in Terms of "Hidden" Variables. *Phys. Rev.* **1952**, *85*, 166.

(138) *Bohmian Mechanics: An Appraisal*; Bohm, D., Cushing, J. T., Fine, A., Goldstein, S., Eds.; Kluwer: Boston, 1996; DOI: 10.1007/978-94-015-8715-0.

(139) Holland, P. R. *The Quantum Theory of Motion*; Cambridge, New York, 1993.

(140) Lopreore, C. L.; Wyatt, R. E. Quantum Wave Packet Dynamics with Trajectories. *Phys. Rev. Lett.* **1999**, *82*, 5190.

(141) Dey, B. K.; Askar, A.; Rabitz, H. A. Multidimensional Wave Packet Dynamics Within the Fluid Dynamical Formulation of the Schrödinger Equation. *J. Chem. Phys.* **1998**, *109*, 8770.

(142) Wyatt, R. E.; Kouri, D. J.; Hoffman, D. K. Quantum Wave Packet Dynamics with Trajectories: Implementation with Distributed Approximating Functionals. *J. Chem. Phys.* **2000**, *112*, 10730.

(143) Bittner, E. R.; Wyatt, R. E. Integrating the Quantum Hamilton-Jacobi Equations by Wavefront Expansion and Phase Space Analysis. *J. Chem. Phys.* **2000**, *113*, 8888.

(144) Wyatt, R. E.; Bittner, E. R. Using Quantum Trajectories and Adaptive Grids to Solve Quantum Dynamical Problems. *Comput. Sci. Eng.* **2003**, *5*, 22.

(145) Iyengar, S. S.; Schlegel, H. B.; Voth, G. A. Atom-Centered Density Matrix Propagation: Generalizations Using Bohmian Mechanics. *J. Phys. Chem. A* **2003**, *107*, 7269.

(146) Bowyer, A. Computing Dirichlet tessellations. *Comput. J.* **1981**, *24*, 162−166.

(147) Sillman, S. Tropospheric Ozone: The Debate over Control Strategies. *Annu. Rev. Energy Env.* **1993**, *18*, 31.

(148) Heard, D. E.; Pilling, M. J. Measurement of OH and HO2 in the Troposphere. *Chem. Rev.* **2003**, *103*, 5163.

(149) Kawaguchi, K. Gas-Phase Infrared Spectroscopy of ClHCl$^-$. *J. Chem. Phys.* **1988**, *88*, 4186.

(150) Boyd, J. P. Defeating the Runge phenomenon for equispaced polynomial interpolation via Tikhonov regularization. *Appl. Math Lett.* **1992**, *5*, 57−59.

(151) Bowman, J. M. personal communication).

(152) Wei, G. W.; Zhang, D. S.; Kouri, D. J.; Hoffman, D. K. Lagrange Distributed Approximating Functionals. *Phys. Rev. Lett.* **1997**, *79*, 775.

(153) Wei, G. W.; Althorpe, S. C.; Zhang, D. S.; Kouri, D. J.; Hoffman, D. K. Lagrange-Distributed Apprixmating-Functional Approach to Wave-Packet Propagation: Application to the Time-Indepdent Wave-Packet Reactant-Product Decoupling Method. *Phys. Rev. A: At., Mol., Opt. Phys.* **1998**, *57*, 3309.

(154) Dell'Accio, F.; Di Tommaso, F. Scattered data interpolation by Shepard's like methods: classical results and recent advances. *Dolomites Research Notes on Approximation* **2016**, *9*, 32−44.

(155) Renka, R. J. Multivariate Interpolation of Large Sets of Scattered Data. *ACM Trans. Math. Softw.* **1988**, *14*, 139−148.